RICE UNIVERSITY

Search for Top Squark via All-Hadronic Decay Channels with Heavy Object Tagging

by

Matthew Cavenaugh Kilpatrick

A Thesis Submitted
in Partial Fulfillment of the
Requirements for the Degree

Doctor of Philosophy

Approved, Thesis Committee:

Karl Ecklund, Chair
Associate Professor of Physics and Astronomy

Paul Padley
Professor of Physics and Astronomy

David Scott
Noah Harding Professor

Houston, Texas

October, 2019

ABSTRACT

Search for Top Squark via All-Hadronic Decay Channels with Heavy Object Tagging

by

Matthew Cavenaugh Kilpatrick

Contents

Bibliography 81

Figures

Tables

Chapter 1

Introduction

1.1 Motivation

Chapter 2

Supersymmetry and the Standard Model

The fundamental theory of particle physics, known as the Standard Model (SM) can predict precise interactions between the fundamental particles in our universe. With these predictions we can confirm processes, but there are some aspects of the universe that have not yet been explained. In this Chapter, we will analyze the Standard Model, look at some specific shortcomings, and introduce supersymmetry as a possible solution.

2.1 The Standard Model

After decades of theoretical and experimental research the SM has been developed into a theory that explains the Electromagnetic (EM), Strong, and Weak forces. The SM has not yet been able to include Gravity within the theory. With the robust theoretical and experimental methods used in the SM, we have discovered new elementary particles and predicted others.

2.1.1 The Fundamental Particles

All visable matter can be explained by three kinds of elementary particles: leptons, quarks, and gauge bosons. Each of these can be distinguished by various quantum properties. The leptons and quarks are fermions, which are particles that have half-integer spin. Leptons are particles that only interact with the EM and

Weak force, while quarks interact with all three forces of the SM. The gauge bosons are the force carries for each respective force and have integer spin.

There are three generations of leptons and quarks which are differentiated by a charge $\pm e$, the charge of an electron. Leptons have three different charged particles: electron (e), muon (μ), and tau (τ), with each charged particle having a corresponding neutrino (ν) of the same flavor, see fig 2.1. Quarks are also separated into three generations of doublets, the down-type $(-\frac{1}{3}e)$: down (d), strange (s), and bottom (b) and up-type $(\frac{2}{3}e)$: up (u), charm (c), and top (t), see fig 2.1. Each of the quarks has a color associated with it which is analogous to an electric charge, except there are three colors charges: red, blue, and green.

2.1.2 Quantum Field Theory

The interactions of all these particles are described by quantized fields whose operators describe the creation and annihilation of particles. Each of the fields of the SM have a corresponding gauge boson, see fig. 2.1. The most well-known being the EM field and its interactions. In order to write a concise theory of the particles in the SM, the symmetry and conservation laws of the SM can be derived by starting with Noether's Theorem.

2.1.3 Noether's Theorem

Noether's theorem states,"to each symmetry of a local Lagrangian, there corresponds a conserved current". This can be done by allowing for an infinitesimal symmetry variation. Requiring the Lagrangian to be invariant under $\phi(x) \rightarrow \phi'(x) = \phi(x) + \alpha\Delta\phi(x)$, where α is infinitesimal real parameter and $\Delta\phi$ is a deformation to

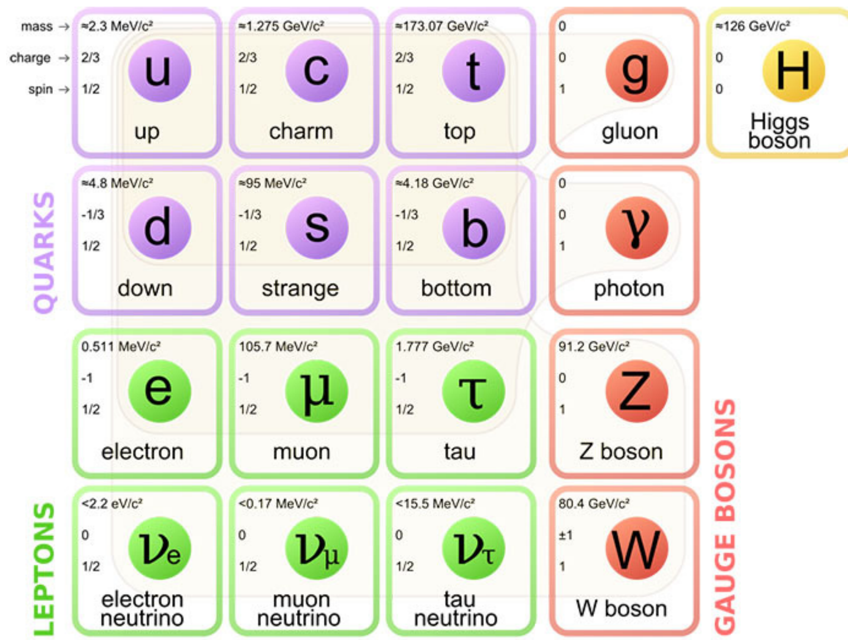

Figure 2.1 : The fundamental particles of the Standard Model. There are three generations of quarks and leptons. Along with the five bosons, where four of them relate to the interactions of the three forces included in the SM: Electromagnetism, the Weak force, and the Strong force and the final being the Higgs boson.

the field, up to a 4-divergance, the Lagrangian transforms as,

$$\mathcal{L}(x) \to \mathcal{L}(x) + \alpha \partial_\mu \mathcal{J}^\mu(x), \tag{2.1}$$

where $\mathcal{J}^\mu$ is a current. If we apply the Euler-Lagrange equation,

$$\partial_\mu(\frac{\partial \mathcal{L}}{\partial(\partial_\mu \phi)}) - \frac{\partial \mathcal{L}}{\partial \phi} = 0, \tag{2.2}$$

to Eqn. 2.1 with the addition of the fluctuation of the particle field. After some simplification we get a conserved current [1, 2],

$$\begin{aligned} \partial_\mu j^\mu(x) &= 0, \text{ where} \\ j^\mu(x) &= \frac{\partial \mathcal{L}}{\partial(\partial_\mu \phi)} \Delta\phi - \mathcal{J}^\mu \end{aligned}. \tag{2.3}$$

We see from the above equation that the current $j^\mu(x)$ of the Lagrangian is conserved. Now let's apply this to the particle fields of the SM.

2.1.4 Quantum Electrodynamics (QED)

First, we start with the assumption that the wave function $\psi(x)$ should transform as,

$$\psi(x) \to e^{i\alpha(x)}\psi(x), \tag{2.4}$$

where $\alpha(x)$ has an arbitrary dependence on space and time. If one were to include this into the Lagrangian for a spin-1/2 particle in a vacuum,

$$\mathcal{L}^{vac}_{QED} = i\overline{\psi}\gamma^\mu \partial_\mu \psi - m\overline{\psi}\psi \tag{2.5}$$

Type	Form	Components	Space Inversion
Scalar	$\overline{\psi}\psi$	1	$+$ under P
Vector	$\overline{\psi}\gamma^{\mu}\psi$	4	Space compts.: $-$ under P
Tensor	$\overline{\psi}\sigma^{\mu\nu}\psi$	6	
Axial Vector	$\overline{\psi}\gamma^{5}\gamma^{\mu}\psi$	4	Space compts.: $+$ under P
Pseudoscalar	$\overline{\psi}\gamma^{5}\psi$	1	$-$ under P

Table 2.1 : A table showing all forms of the fermion currents. These can be symmetric under parity transformation in all or some components.

where the γ^{μ} are the Dirac matrices, ∂_{μ} is the partial derivative, $\overline{\psi}$ is the hermitian conjugate of the wavefuntion ψ, and m is the mass of the particle. As a small aside, the bilinear quantities $\overline{\psi}(4{\times}4)\psi$ have certain properties under lorentz transformations when the 4×4 matix is a γ-matrices. These are of the form,

$$\gamma^0 = \begin{bmatrix} \boldsymbol{I} & 0 \\ 0 & -\boldsymbol{I} \end{bmatrix}, \boldsymbol{\gamma} = \begin{bmatrix} 0 & \boldsymbol{\sigma} \\ -\boldsymbol{\sigma} & 0 \end{bmatrix}, \gamma^5 = \begin{bmatrix} 0 & \boldsymbol{I} \\ \boldsymbol{I} & 0 \end{bmatrix} \tag{2.6}$$

where the $\boldsymbol{I}$ is the identity matrix and $\boldsymbol{\sigma}$ are the Dirac matrices. We can combine the first two parts of Eqn. 2.6 and write it compactly as γ^{μ} where $\mu = 0, 1, 2,$ and 3. The possible interesting quantities of the above transformations are shown in Table 2.1.

To allow for the field to be invariant, we must include a derivative, D_{μ}, that is covariant under phase transformations,

$$D_{\mu} \equiv \partial_{\mu} - ieA_{\mu}. \tag{2.7}$$

Figure 2.2 : The possible feynman diagrams in QED. The e can be replaced with any spin-1/2 charged particle. We see that the electron and photon can propagate freely in space or a vertex with one photon and a particle-antiparticle pair is allowed.

The covariant derivative includes the vector field A_μ which must also transform as,

$$A_\mu \rightarrow A_\mu + \frac{1}{e}\partial_\mu \alpha. \tag{2.8}$$

So after requiring that there be a local gauge transformation, we were forced to introduce a vector field A_μ, called the gauge field, which couples to Dirac particles in the same way as the photon field. We will think of this new field as the real photon field, which means we need to add a kinematic energy portion to the lagrangian. This kinematic term will be invariant under Eqn. 2.8, which leads us to final representation of the QED lagrangian which can be written down concisely as,

$$\mathcal{L}_{QED} = \overline{\psi}(i\gamma^\mu \partial_\mu - m)\psi + e\overline{\psi}\gamma^\mu A_\mu \psi - \frac{1}{4}F^{\mu\nu}F_{\mu\nu}, \tag{2.9}$$

where A_μ is the EM field operator and $F^{\mu\nu}$ is the EM field tensor. This Lagrangian describes the interactions between spin-1/2 charged particles and the $U(1)$ EM force. Each of the parts of this equation are lorentz invariant which allows this to be true in all reference frames.

From the QED Lagrangian Eqn. 2.9, we see that particles that interact electromagnetically can interact with the photon. This can be shown as a feynman diagram, see Fig. 2.2, which has a vertex interaction with a photon and a particle-antiparticle pair. These, and the inclusion of freely moving particles, are the basic types of feynman diagrams for QED.

2.1.5 Quantum Chromodynamics

Let's now transition from the description of the $U(1)$ EM field to the $SU(3)$ Quantum Chromodynamic (QCD) field and the transformation of quark fields. A quark in a vaccuum is described by,

$$\mathcal{L}_{QCD}^{vac} = \overline{q}_j(i\gamma^\mu \partial\mu - m)q_j, \tag{2.10}$$

where q_1, q_2, and q_3 are the three color fields. From this we want to require that the field is again invariant under another local phase transformation such as,

$$q(x) \rightarrow Uq(x) \equiv e^{i\alpha_a(x)T_a}q(x), \tag{2.11}$$

where U is a 3×3 unitary matix, T_a with $a = 1, \ldots, 8$ are a set of linearly independent traceless 3×3 matrices, and α_a are the group parameters. Since the generators T_a do not necessarily commute with each other, we can see that it is a non-Abelian transformation and the commutator can be represented as,

$$[T_a, T_b] = if_{abc}T_c, \tag{2.12}$$

where f_{abc} are constants.

We need to impose $SU(3)$ local gauge invariance on Eqn. 2.10, to allow for the following phase transformations,

$$\begin{aligned} q(x) &\rightarrow (1 + i\alpha_a(x)T_a)q(x), \\ \partial_\mu q &\rightarrow (1 + i\alpha_a T_a)\partial_\mu q + iT_a q \partial_\mu \alpha_a. \end{aligned} \tag{2.13}$$

From this is seems straight forward that we can proceed in exactly the same manner as QED, which is to add a transformation to the derivative,

$$D_\mu = \partial_\mu + ig_Q T_a G^a_\mu. \tag{2.14}$$

where the field G^a_μ transforms as,

$$G^a_\mu \rightarrow G^a_\mu - \frac{1}{g_Q}\partial_\mu \alpha_a, \tag{2.15}$$

where g_Q is the coupling strength of QCD interactions. This will give us a similar Lagrangian to the QED one described above, but this is not sufficient for a non-Abelian gauge transformation and it does not produce a gauge-invariant Lagrangian. One final transformation is required for the G^a_μ fields,

$$G^a_\mu \rightarrow G^a_\mu - \frac{1}{g_Q}\partial_\mu \alpha_a - f_{abc}\alpha_b G^c_\mu. \tag{2.16}$$

This finally gives us a gauge invariant kinetic energy term for all the G^a_μ fields and thus we can write the QCD interactions as,

$$\mathcal{L}_{QCD} = \overline{q}(i\gamma^\mu \partial_\mu - m)q - g_Q(\overline{q}\gamma^\mu T_a q)G^a_\mu - \frac{1}{4}G^a_{\mu\nu}G^{\mu\nu}_a. \tag{2.17}$$

From the QCD Lagrangian Eqn. 2.17, we can see that it includes all of the same interactions we showed for QED, but must be color neutral. However, QCD also

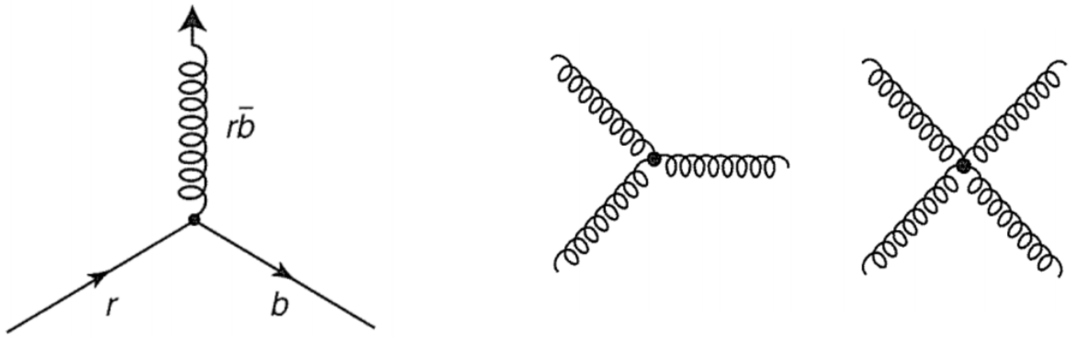

Figure 2.3 : The possible feynman diagrams in QCD. Each vertex needs to be color neutral. Here is just an example of a red-blue vertex. QCD also includes a 3- and 4-vertex with gluons.

included a 3- and 4-vertex interaction between the gluons, which arises due to the non-abelian nature of the force. From this, it is easy to tell that QCD is a much more complicated theory. We seem to be missing a vital part of the SM, specifically a theory for the Weakly interacting processes which is mediated by the massive bosons, W and Z from fig. 2.1.

2.1.6 Weak Force

The Weak force is responsible for nuclear decay. The Weak force has an interaction of the type $\frac{1}{2}\gamma^{\mu}(1-\gamma^{5})$ so it is a V-A interaction with $SU(2)$ symmetry. From this, we can conclude that it violates Parity. Parity is a transformation from $(x, y, z) \rightarrow (-x, -y, -z)$ or space inversion. Since it violates Parity, the next step is to consider a conservation of CP, where C is charge conjugation (particle-to-antiparticle).

The main experimental implications of this proposed conservation comes from the decay of the neutral Kaon, $K^0(\bar{s}d)$ and $\overline{K}^0(s\bar{d})$. These have two CP states which are,

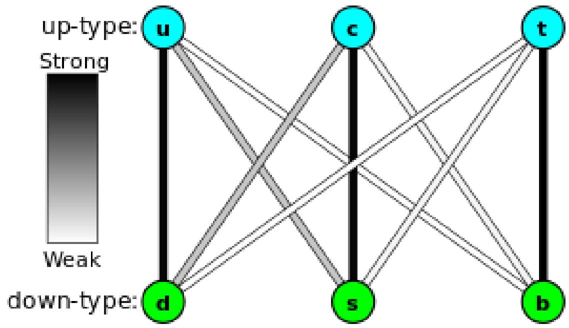

Figure 2.4 : A gramatical representation to show the couplings for Weak interactions, known as the Cabibbo-Kobayashi-Maskawa Matrix.

$CP\,|K^0\rangle = -\,|\overline{K}^0\rangle$, and $CP\,|\overline{K}^0\rangle = -\,|K^0\rangle$. Once we normalize these eigenstates of CP we get the corresponding wavefunctions,

$$|K_1\rangle = \left(\frac{1}{\sqrt{2}}\right)(|K^0\rangle - |\overline{K}^0\rangle) \text{ and } |K_2\rangle = \left(\frac{1}{\sqrt{2}}\right)(|K^0\rangle + |\overline{K}^0\rangle), \tag{2.18}$$

where each has the invariance $CP\,|K_1\rangle = |K_1\rangle$ and $CP\,|K_2\rangle = -\,|K_2\rangle$. The two Kaon states are expected to decay into either two pions or three pions for $|K_1\rangle$ and $|K_2\rangle$, respectively. Since there is a greater energy release in the $|K_1\rangle$ state the lifetime of that particle is thought to be less than $|K_2\rangle$. After experimenting on the purity of Kaon decays after a long distance away from an interaction point, we have found that it is possible for the $|K_1\rangle$ to decay into three pions. This is direct evidence of Weak decays violating CP conservation.

Now the Weak force is mediated by two vector bosons, W and Z, see fig. 2.1. These are unlike the other forces because these vector bosons have a large mass of $m_W = 80.379 \pm 0.012$ GeV and $m_Z = 91.1876 \pm 0.0021$ GeV. The W boson is a charged particle and interacts with many nuclear decays.

The W boson interacts very interestingly for quarks in the SM. There is a mixing of flavors of quarks for particles. They will mix partners between up-type and down-type particles, see fig. 2.4. [Kobayashi, M. and Maskawa, K. (1973) Progress in Theoretical Physics, 49, 652]. The interactions for the generalized three generations of quarks is known as the Cabibbo-Kobayashi-Maskawa (CKM) matrix,

$$\begin{bmatrix} d' \\ s' \\ b' \end{bmatrix} = \begin{bmatrix} V_{ud} & V_{us} & V_{ub} \\ V_{cd} & V_{cs} & V_{cb} \\ V_{td} & V_{ts} & V_{tb} \end{bmatrix} \begin{bmatrix} d \\ s \\ b \end{bmatrix}, \tag{2.19}$$

where for example, V_{ud} is the coupling of u to d which is exactly $(d \rightarrow u + W^-)$. This matrix can be reduced to a form which has three generalized Cabibbo angles $(\theta_{12}, \theta_{23}, \theta_{13})$ and a phase factor (δ). The coupling between the third generation does not mix with the other two generations. From that we can recover the Cabibbo-GIM matrix[cite here]. For the moment, we can only determine these values from experimentation.

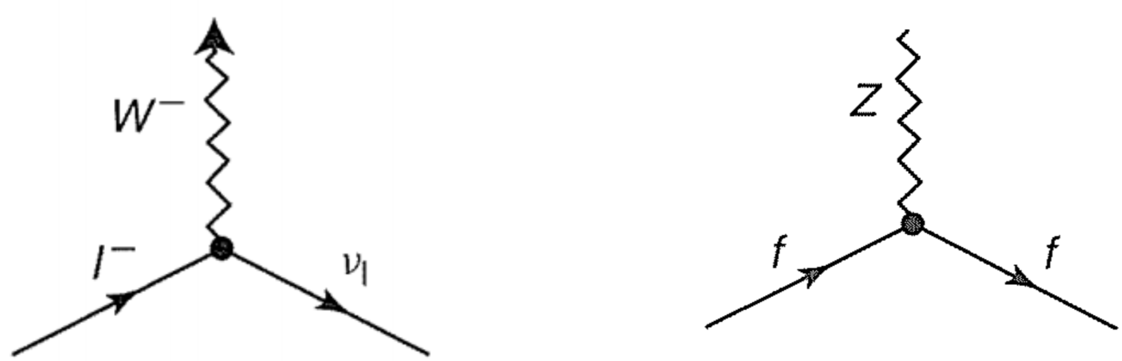

Figure 2.5 : Feynman diagram for Neutral Weak interaction and the charged weak current.

The Z boson is known as the neutral current. This boson mediates forces between particles and their respective antiparticles, see fig. **??**. This interaction for the neutral weak force is $\gamma^\mu(c_V^f - c_A^f\gamma^5)$ which is quite similar to the charged weak interaction, but differs by the constants c_V^f and c_A^f. The Weak interactions are shown in Fig. 2.5. We see the charged W boson interactions with the charged leptons and their respective neutrinoes or allows for flavor changing interactions with quarks. The neutral Z boson interacts in the same way as the photon.

2.1.7 The Electroweak Lagrangian

The simplest group for the Electroweak interaction is $SU(2)_L \times U(1)_Y$ which will give the left-handed interactions in doublets with the addition of massive gauge bosons W and Z with a massless photon. We first consider the free Lagrangian,

$$\mathcal{L} = \overline{\psi}_j\gamma^\mu\psi_j, \tag{2.20}$$

where j is the fermion wavefunction. We are not including the mass parameter because it would cause the left and right-handed parts to mix. This is assumed to transform under the global invariant

$$\begin{aligned} \chi_L &\to \chi_L' = e^{i\frac{\tau_a}{2}\alpha^a(x)+i\beta(x)Y}\chi_L, \\ \psi_R &\to \psi_R' = e^{i\beta(x)Y}\psi_R \end{aligned} \tag{2.21}$$

where the transformation $e^{i\frac{\tau_a}{2}\alpha^a(x)}$ with $a = 1, 2, 3$ is the $SU(2)_L$ transformation and only acts on the left-handed doublet. The next step is to require that the Lagrangian is invariant under local $SU(2)_L \times U(1)_Y$. We allow for the following covariant derivatives,

$$
\begin{aligned}
D_\mu\psi_1 &= [\partial_\mu - ig_W\frac{\tau_a}{2}W^a_\mu - ig'_W y_1 B_\mu]\psi_1 \\
D_\mu\psi_2 &= [\partial_\mu - ig'_W y_2 B_\mu]\psi_2 \\
D_\mu\psi_3 &= [\partial_\mu - ig'_W y_3 B_\mu]\psi_3
\end{aligned}
\tag{2.22}
$$

where g_W and g'_W are the Weak force coupling constants while W^a_μ and B_μ are four gauge bosons and can be the possible candidates for $W^\pm$, $Z$and γ.

Just like the above descriptions the fields need to transform along with the wave-funtions and derivatives. These transformations are,

$$
\begin{aligned}
B_\mu \rightarrow & B'_\mu = B_\mu + \frac{1}{g'_W}\partial_\mu\beta(x) \\
W\mu \rightarrow & W'_\mu = U_L W_\mu U_L^\dagger - \frac{1}{g_W}\partial_\mu U_L U_L^\dagger
\end{aligned}
\tag{2.23}
$$

where $U_L = e^{i\frac{\tau_a}{2}\alpha^a(x)}$. These transformation are similar to the QED and QCD transformation. If we include all of these invariant transformations in the free Weak Lagrangian Eqn. 2.20 and we get a free invariant Lagrangian, but this does not allow us to include a mass term for the fermions. Therefore this is not a viable procedure to include the Electroweak interactions into the model. In order to do this we must include the Higgs Mechanism.

2.1.8 The Higgs Mechanism

We are interested in the spontaneous symmetry breaking of a local $SU(2)$ group. Specifically, the following Lagrangian,

$$
\mathcal{L} = (\partial_\mu\phi)^\dagger(\partial^\mu\phi) - \mu^2\phi^\dagger\phi - \lambda(\phi^\dagger\phi)^2, \tag{2.24}
$$

with ϕ being a $SU(2)$ doublet of complex scalar fields,

$$\phi = \frac{1}{2}\begin{bmatrix}\phi_1 + i\phi_2 \\ \phi_3 + i\phi_4\end{bmatrix} \tag{2.25}$$

and is invariant under global $SU(2)$ phase transformations $\phi \to e^{i\alpha_a \tau_a/2}\phi$. To allow for local invariance, we first allow for a covariant derivative,

$$D_\mu = \partial_\mu + ig_W \frac{\tau_a}{2} W^a_\mu, \tag{2.26}$$

where we now have three gauge fields, W^a_μ. If we assume an infanitesimal gauge transformation for the $SU(2)$ doublet $\phi(x) \to \phi'(x) = (1 + i\frac{\tau_a}{2}\alpha^a(x))\phi(x)$, then the gauge fields will transform as,

$$W^a_\mu \to W^a_\mu - \frac{1}{g_W}\partial_\mu \alpha_a - f_{abc}\alpha_b W^c_\mu. \tag{2.27}$$

You can see that Eqn. 2.27 is similar to Eqn. 2.16 where we have replaced the QCD gauge field with the three gauge fields W^a_μ. If we include these locally invariant transformations into the above $SU(2)$ Lagrangian we get,

$$\mathcal{L} = (\partial_\mu \phi + ig_W \frac{1}{2}\tau_a W^a_\mu \phi)^\dagger(\partial^\mu \phi + ig_W \frac{1}{2}\tau_a W^{a\mu}\phi) - \mu^2 \phi^\dagger \phi + \lambda(\phi^\dagger\phi)^2 - \frac{1}{4}W^a_{\mu\nu}W^{a\mu\nu}, \tag{2.28}$$

where the gauge field kinetic term has been included at the end. The most interesting regions of this Lagrangian is when $\mu^2 < 0$ and $\lambda > 0$, and the potential has a minimum at $\phi^\dagger\phi = -\frac{\mu^2}{2\lambda}$. With this we will expand the potential around the minimum and require that,

$$\phi_1 = \phi_2 = \phi_4 = 0, \phi_3^2 = -\frac{\mu^2}{2\lambda} \equiv v^2. \tag{2.29}$$

This is the spontaneous symmetry breaking of the $SU(2)$ symmetry, because of this we are able to substitute an expansion for the field,

$$\phi = \sqrt{\frac{1}{2}} \begin{bmatrix} 0 \\ v + h(x) \end{bmatrix} \tag{2.30}$$

with this specific transformation of the $SU(2)$ doublet and the simplification of Eqn. 2.28, the only remaining field is $h(x)$ which is refered to as the Higgs field. This is what is known as the Higgs Mechanism for a $SU(2)$ symmetry.

2.1.9 Electroweak

We want to include the Higgs Mechanism into the weak isospin and weak hypercharge, $SU(2)_L \times U(1)_Y$, transformations of electoweak interactions. Isospin and hypercharge is defined as $I_3 = \frac{1}{2}(n_u - n_d)$ and $Y \equiv B + S$, respectfully, where n_u, n_d is the number of up or down quarks, B is the baryon number, and S is the strangeness. The weak isospin triplet for weak currents can be written down using Eqn. 2.28,

$$J^i_\mu(x) = \overline{\chi}_L \gamma_\mu \frac{1}{2} \tau_i \chi_L, \text{ with } i = 1, 2, 3. \tag{2.31}$$

Since this is a current we can calculate the charge by integrating of all of space, $T^i = \int J^i_0(x) d^3x$, which will give us the generators of the $SU(2)_L$ symmetry $[T^i, T^j] = i\epsilon_{ijk} T^k$. Weak hypercharge, Y, is then defined by $Q = T^3 + \frac{Y}{2}$ where Q is the charge and T^3 is the third component of the weak isospin. The weak hypercharge is a conserved quantity of the $U(1)_Y$ symmetry.

First, we need to include the coupling of the Weak current J^a_μ and the gauge field $W^{a\mu}$ such that,

$$-ig_W J^a_\mu W^{a\mu} = -ig_W \overline{\chi}_L \gamma_\mu T^a W^{a\mu} \chi_L \tag{2.32}$$

which is the basic interaction for the $SU(2)_L$ symmetry. Then, we also need to include the weak hypercharge current with the fourth vector boson B^μ,

$$-i\frac{g'_W}{2}j^Y_\mu B^\mu = -ig'_W\overline{\psi}\gamma_\mu\frac{Y}{2}\psi B^\mu, \tag{2.33}$$

here the operators T^a and Y are generators for the $SU(2)_L$ and $U(1)_Y$ gauge transformations, respectively. Now we combine the two symmetries with the transformations of the left and right hand components of ψ and from this we can write down the contributions of the two gauge fields W^3_μ and B_μ and the mising angle θ_W to find the interactions of the two neutral currents. The physical fields are thus,

$$-ig_W J^3_\mu W^{3\mu} - i\frac{g'_W}{2}j^Y_\mu B^\mu = -iej^{em}_\mu A^\mu - \frac{ie}{sin\theta_W cos\theta_W}[J^3_\mu - sin^2\theta_W j^{em}_\mu]Z^\mu. \tag{2.34}$$

From this we can write down the Electroweak Lagrangian, for any fermion that interacts with the field. Moreover, we can formulate the Higgs mechanism, such that we can calculate the theoretical masses of the gauge bosons and fermions as,

$$\begin{aligned} M_W &= \frac{1}{2}vg_W \\ M_Z &= \frac{1}{2}v\sqrt{g^2_W + g'^2_W}, \end{aligned} \tag{2.35}$$

but these masses cannot be predicted since they depend on the values from the chosen Higgs field.

2.1.10 The Standard Model Lagrangian

With the inclusion of the Higgs mechanism and the formulation of a local gauge invariant Lagrangian for the Electroweak and QCD fields, we have the complete SM

Lagrangian as,

$$\begin{aligned}\mathcal{L} =& -\frac{1}{4}W^a_{\mu\nu}W^{a\mu\nu} - \frac{1}{4}B_{\mu\nu}B^{\mu\nu} - \frac{1}{4}G^a_{\mu\nu}G^{\mu\nu}_a \\ &+ \overline{L}\gamma^\mu(i\partial_\mu - g_W\frac{1}{2}\tau^a W^a_\mu - g'_W\frac{Y}{2}B_\mu - g_Q T_b G^b_\mu)L \\ &+ \overline{R}\gamma^\mu(i\partial_\mu - g'_W\frac{Y}{2}B_\mu - g_Q T_b G^b_\mu)R \\ &+ |(i\partial_\mu - g_W\frac{1}{2}\tau^a W^a_\mu - g'_W\frac{Y}{2}B_\mu)\phi|^2 - V(\phi) \\ &- (G_1\overline{L}\phi R + G_2\overline{L}\phi_c R + \text{hermitian conjugate}),\end{aligned} \tag{2.36}$$

where the first terms are the kinetic energies and self-interactions of the $W^\pm, Z, g,$ and γ bosons, the second and third terms are the kinetic energies and interactions of the leptons and quarks with the $W^\pm, Z, g,$ and γ bosons where L is a left-handed fermion doublet and R is a right-handed fermion singlet. The fourth term is the $W^\pm, Z, \gamma$ and Higgs masses and couplings. The final term is the lepton and quark masses and couplings to the Higgs field.

2.2 Fundamental Problems in the Standard Model

The SM is able to accurately and precisely describe many facets of the universe. Whether it comes to predicting the existence of a sixth quark or the confirmation of $g-2$ for the muon to 9 orders of magnitude. Unfortunately, there is some evidence of matter or interactions that cannot be described such as dark matter, the Hierarchy problem, and a possible grand unified theory. Let's look into each of these further.

2.2.1 Dark Matter

The main motivation for Dark Matter is the difference between the visible matter and the measureable matter in the universe. This has most notably been seen in the

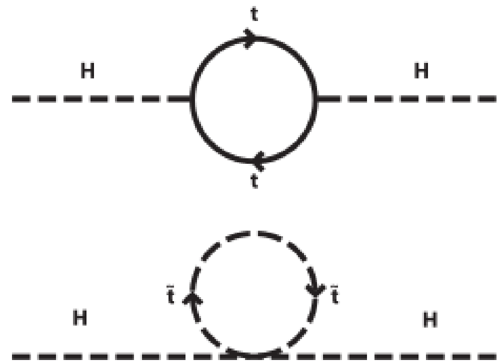

Figure 2.6 : The loop corrections to the Higgs boson interacting with a top quark and its superpartner the top squark. This is a next-to-leading order (NLO) correction to the Higgs boson mass.

radial velocities of stars in galaxies. In a galaxy which is solely made up of visible matter, matter that interacts with light, the radial velocity of stars should decrease as $1/\sqrt{r}$ the further away it is from the galactic nuclei, although measurements show the velocity becoming constant as a function of radius.

The original study of this was from the galaxy NGC 1560, where the measured galactic velocity curve provided a result that was 400 times large than the visible matter in the cluster (A. H. Broeils Astron. and Astrophys. 256 19 (1992)). To reproduce these features in models, the mass of the galaxy must be significantly more than what is seen. This implies some unseen dark matter, that still interacts with the gravitational field but not with the EM field. There is currently no such particle in the SM that has these properties.

2.2.2 Hierarchy Problem

The Higgs boson is a beautiful solution to electroweak symmetry breaking and gives a method for particles to acquire mass, see Sec. 2.1.8, and was discovered to have a measured mass of $m_H = 125.18 \pm 0.16$ GeV [3]. This value though is not predictable with the SM and leads to some inconsistencies when you include loop corrections. Since the Higgs is strongly coupled to particles with large masses, the dominant loop correction is due to interactions with the t quark. These higher order loop corrections to the Higgs mass, m_H^2, caused by the fermionic t loop, see fig 2.6, are,

$$\Delta m_H^2 = -\frac{|\lambda_t|^2}{8\pi^2}\Lambda_{UV}^2 + \cdots, \tag{2.37}$$

where λ_f is the vertex factor for the respective fermion and Λ_{UV} is the ultraviolet momentum cutoff. The Higgs boson loop corrections are highly dependent on all virtual and real particles that couple to the Higgs field, we can see the corrections from Eqn. 2.37 from the t quark will cause a large divergence. The quadratic divergence of the Higgs mass is only renormalizable with a fine tuning of the parameters λ_f and Λ_{UV}.

This means the only way for the SM to reconcile this unfortunate fact is to have a relatively lucky cancellation of very large numbers of order 10^{32} with equally small numbers. Fortunately, if we add the contribution of a bosonic partner of the fermion the Higgs loop corrections reduce to,

$$\Delta m_H^2 = \frac{\lambda_S}{16\pi^2}[\Lambda_{UV}^2 - 2m_S^2 ln(\Lambda_{UV}/m_S) + \cdots]. \tag{2.38}$$

With the introduction of a scalar partner to the t, there is a logarithmic divergence to the higgs boson mass and can be renormalized through the normal methods.

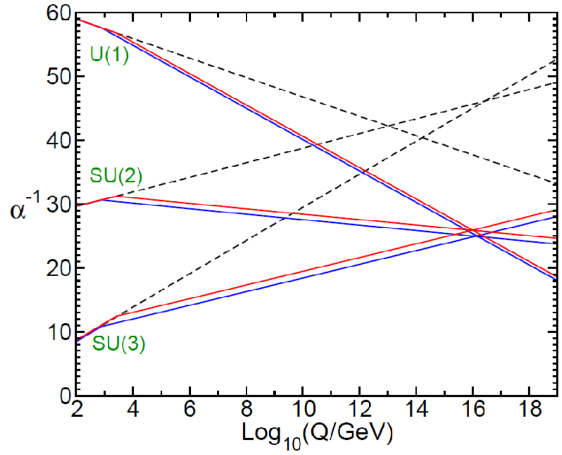

Figure 2.7 : The energy dependence of the inverse gauge couple of each force in the SM (dashed line) and the MSSM (solid lines). The MSSM gives two thresholds for the sparticle mass 750 GeV and 2.5 TeV.

2.2.3 Grand Unified Theory

The SM is able to accurately describe three of the fundamental sources at typical energy scales, 1 to 10^4 GeV, but idealy the forces would be able to merge into a single force at higher energies. This has not been directly observed, but many theories, such as supersymmetry (SUSY), predict its existence [4].

At standard energies for particle physics experiments the difference in the strength of each force is quite noticeable. But it has been shown that in the SM the strengths of each force are dependent on the energy scale and it would be ideal that they converge to a single force at large energies, such as 10^{16} GeV. In fig. 2.7, we see the extrapolated energy scales of the forces in the SM shown as the dotted line. These unfortunately, do not meet at a single point to become one force, but if we include supersymmetry into the model we get a nice convergence between the forces [4].

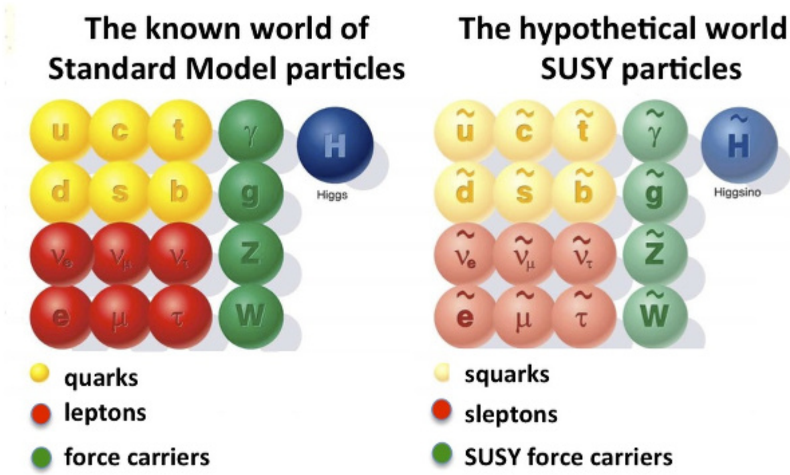

Figure 2.8 : The corresponding SUSY particles which are partners to the SM particles.

2.3 Supersymmetry

We have seen from the above three problems that there is still more to learn. Some of the features of the universe, such as; dark matter, the hierarchy problem, and a grand unified theory have not been explained. We saw from the Hierarchy problem that the addition of a bosonic partner to a fermion will allow for the loop corrections to be renormalizable without fine tuning. Fortunately, some theories have allowed for such a problem to be solved. Namely the theory of SUSY which essentially states that each particle in the SM has a superpartner that has only the spin changed, that every fermion has a bosonic partner that has all the same quantum numbers except the spins differ by 1/2, and vice-versa.

The partners to the fermions are denoted with a 's' in front of the name to notify that it is the scalar form of the particle and the partners to the bosons have an 'ino' attached at the end, such as photino, gluino, wino, and Higgsino. So for the partners to the fermionic particles in the standard model we have: sup ($\widetilde{u}$), sdown ($\widetilde{d}$), scharm ($\widetilde{c}$), sstrange ($\widetilde{s}$), stop ($\widetilde{t}$), and sbottom ($\widetilde{b}$) for the squarks and selectron ($\widetilde{e}$), smuon ($\widetilde{\mu}$), and stau ($\widetilde{\tau}$) for the charged sleptons. The partners to the neutrinos, which are always left-handed if you neglect the minimal masses, are sneutrinos ($\widetilde{\nu}_e, \widetilde{\nu}_\mu, \widetilde{\nu}_\tau$), where whe have one for each flavor of lepton, see Fig. 2.8.

If the SUSY was unbroken the superpartners would have exactly the same properties as the SM pairs except their spin. This would cause a massless photino or a $m_{\widetilde{e}} = 0.511$ keV selectron. These particles would certainly have been detected at this point, which leads us to think that SUSY is a broken symmetry where all the superpartners have a mass that is significantly higher than their SM partners.

2.3.1 Supermultiplets and Chirality

A supermultiplets is any symmetry where the number of bosonic degrees of freedom and fermionic degrees of freedom are equal, $n_B = n_F$. The simplest way to achieve this is to have a combination of a single Weyl fermion, which is a chiral representation of the fermion and has two spin helicity states, $n_F = 2$, and two real scalars with each having $n_B = 1$. It becomes convenient for the mathematics to combine the two real scalars into one complex scalar field. Now the combination of a complex scalar field and a Weyl fermion is known as a chiral supermultiplet.

2.3.2 Minimal Supersymmetric Standard Model

We have discussed how the fermions transform under the rules of SUSY, but how do the scalar field mediators translate into this new framework. First, lets look at the Higgs boson. We know that there is not only one chiral supermultiplet. If there was only one in the electroweak gauge symmetry, with a Higgsino of spin-1/2, would

Names		spin 0	spin 1/2	$SU(3)_C$, $SU(2)_L$, $U(1)_Y$
squarks, quarks	Q	$(\widetilde{u}_L \ \ \widetilde{d}_L)$	$(u_L \ \ d_L)$	$(\,\mathbf{3},\ \mathbf{2}\,,\ \frac{1}{6})$
($\times 3$ families)	$\overline{u}$	$\widetilde{u}^*_R$	$u^\dagger_R$	$(\,\overline{\mathbf{3}},\ \mathbf{1},\ -\frac{2}{3})$
	$\overline{d}$	$\widetilde{d}^*_R$	$d^\dagger_R$	$(\,\overline{\mathbf{3}},\ \mathbf{1},\ \frac{1}{3})$
sleptons, leptons	L	$(\widetilde{\nu}\ \widetilde{e}_L)$	$(\nu \ \ e_L)$	$(\,\mathbf{1},\ \mathbf{2}\,,\ -\frac{1}{2})$
($\times 3$ families)	$\overline{e}$	$\widetilde{e}^*_R$	$e^\dagger_R$	$(\,\mathbf{1},\ \mathbf{1},\ 1)$
Higgs, higgsinos	H_u	$(H_u^+ \ \ H_u^0)$	$(\widetilde{H}_u^+ \ \ \widetilde{H}_u^0)$	$(\,\mathbf{1},\ \mathbf{2}\,,\ +\frac{1}{2})$
	H_d	$(H_d^0 \ \ H_d^-)$	$(\widetilde{H}_d^0 \ \ \widetilde{H}_d^-)$	$(\,\mathbf{1},\ \mathbf{2}\,,\ -\frac{1}{2})$

Table 2.2 : The chiral supermultiplets of the MSSM. Spin-0 fields are complex scalars and spin-1/2 fields are left-handed two component Weyl fermions [4].

Names	spin 1/2	spin 1	$SU(3)_C$, $SU(2)_L$, $U(1)_Y$
gluino, gluon	$\widetilde{g}$	g	$(\,\mathbf{8},\ \mathbf{1}\,,\ 0)$
winos, W bosons	$\widetilde{W}^\pm \ \ \widetilde{W}^0$	$W^\pm \ \ W^0$	$(\,\mathbf{1},\ \mathbf{3}\,,\ 0)$
bino, B boson	$\widetilde{B}^0$	B^0	$(\,\mathbf{1},\ \mathbf{1}\,,\ 0)$

Table 2.3 : The chiral supermultiplets of the MSSM [4].

not have the anomaly cancellation of the traces, $Tr[T_3^2 Y] \neq 0$ and $Tr[Y^3] \neq 0$, where T_3 is the third component of weak isospin and Y is the weak hypercharge. In the SM, the traces of these for the fermions are already satified. So we must include two chiral supermultiplets of the Higgsino, with $Y = \pm\frac{1}{2}$, see table 2.2.

It turns out that this is also necessary for the Higgsino to give mass to different particles in the SM. A Higgs boson with $Y = 1/2$ has the Yukawa couplings that allow it to interact with the up-type quarks (u, c, t). Only a Higgs boson with $Y = -1/2$ has the correct Yukawa couplings to interact with the down-type quarks (d, s, b) and the charged leptons (e, μ, τ).

The SM vector boson will also have a corresponding chiral supermultiplet. They have fermionic superpartners that are referred to as gauginos. For the $SU(3)_C$ color gauge interactions of QCD, which are a spin-1/2 color-octet, has a partner called a gluino ($\widetilde{g}$). The electroweak gauge theory $SU(2)_L \times U(1)_Y$ has the superpartners $\widetilde{W}^+, \widetilde{W}^0, \widetilde{W}^-$, and $\widetilde{B}^0$ each with spin-1/2, called winos and bino, see table 2.3. The gaugino mixtures of $\widetilde{W}^0$ and $\widetilde{B}^0$ give the corresponding zino ($\widetilde{Z}^0$) and photino ($\widetilde{\gamma}$). The chiral supermultiplets shown in table 2.2 and 2.3 give the particles of the Minimal Supersymmetric Standard Model (MSSM).

The five higgsinos and electroweak gauginos mix with each other to because of electroweak symmetry breaking [4]. The neutral higgsinos ($\widetilde{H}_u^0$ and $\widetilde{H}_d^0$) and neutral gauginos ($\widetilde{B}$ and $\widetilde{W}^0$) mix into four mass eigenstates, which are called neutralinos, $\widetilde{\chi}_1^0, \widetilde{\chi}_2^0, \widetilde{\chi}_3^0$, and $\widetilde{\chi}_4^0$. The charged higgsinos ($\widetilde{H}_u^+$ and $\widetilde{H}_d^-$) and charged gauginos ($\widetilde{W}^+$ and $\widetilde{W}^-$) can mix into two mass eigenstates with charge ± 1 called charginos, $\widetilde{\chi}_1^\pm$ and $\widetilde{\chi}_2^\pm$.

2.3.3 R Parity

R-parity or matter parity is the multiplicatively conserved quantum number defined as,

$$P_R = (-1)^{3(B-L)+2s}, \tag{2.39}$$

where B is the baryon number, L is the lepton number, and s is the spin of the particle. From this we can find the R-parity of all the particles in the SM and MSSM. The definition of R-parity is quite useful because all the particles of the SM have an R-partity of $P_R = +1$, while all of the squarks, sleptons, gauginos, and higgsinos have $P_R = -1$.

R-parity is thought to be exactly conserved in SUSY, where there is no mixing between particles ($P_R = +1$) and sparticles ($P_R = -1$). This leads to three important

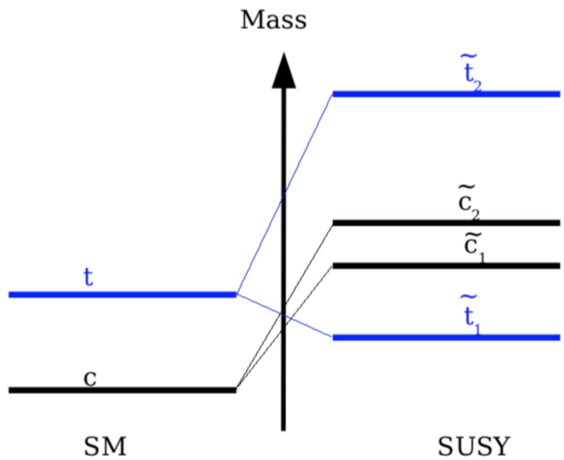

Figure 2.9 : On the right we have the arbitrary masses of the top and charm quarks. The left and right handed states mix into two mass eigenstates. It is possible that the top squark will have the smallest mass of the squarks.

consequences:

- The lightest sparticle that has $P_R = -1$ is called the "lightest supersymmetric particle" or LSP, which must be absolutely stable. If it is electrically neutral, it is a possible non-baryonic dark matter candidate.

- Every sparticle, other than the LSP, must eventually decay into an odd number of LSPs.

- For collider experiments, sparticles will only be produced in even numbers.

We are going to be investigating a MSSM that conserves R-parity. This is quite well motivated by the possiblilty of a dark matter candidate.

2.3.4 Mass Spectrums

The third family of squarks and sleptons should have quite different masses compared to their first- and second-family counterparts, which is caused by the large Yukawa (y_t, y_b, y_τ) and soft (a_t, a_b, a_τ) couplings, which are holomorphic parameters proportional to the Yukawa couplings. This causes significant mixing between the chiral superpartners $(\widetilde{t}_L, \widetilde{t}_R), (\widetilde{b}_L.\widetilde{b}_R)$, and $(\widetilde{\tau}_L, \widetilde{\tau}_R)$. We will concentrate on how the mass of the top squark, $\widetilde{t}$ evolves in the MSSM. Given many contributions to the top squark mass such as; squared-mass terms, 4-vertex interactions terms with the up-type Higgs, the 3-vertex interactions with the down-type Higgs, and scalar potential couplings. We have a square-mass matrix for the top squarks,

$$\mathcal{L}_{\text{stop masses}} = - \begin{bmatrix} \widetilde{t}_L^* & \widetilde{t}_R^* \end{bmatrix} \boldsymbol{m_{\widetilde{t}}^2} \begin{bmatrix} \widetilde{t}_L \\ \widetilde{t}_R \end{bmatrix} \tag{2.40}$$

where

$$\boldsymbol{m_{\widetilde{t}}^2} = \begin{bmatrix} m_{Q_3}^2 + m_t^2 + (\frac{1}{2} - \frac{2}{3} sin^2\theta_W) cos(2\beta) m_Z^2 & v(a_t^* sin\beta - \mu y_t cos\beta) \\ v(a_t sin\beta - \mu^* y_t cos\beta) & m_{\overline{u}_3}^2 + m_t^2 + (\frac{2}{3} sin^2\theta_W) cos(2\beta) m_Z^2 \end{bmatrix}. \tag{2.41}$$

This is a hermitian matrix and can be diagonalized to give eigenstates $\widetilde{t}_1$ and $\widetilde{t}_2$ which are linear combinations of the left and right-handed $\widetilde{t}$, see fig. 2.9. Now we get the eigenvalues for the mass states as $m_{\widetilde{t}_1}^2 < m_{\widetilde{t}_2}^2$. From this models predict that the $\widetilde{t}_1$ is the lightest squark [4].

2.3.5 Supersymmetry Searches

The SM of particle physics has been a powerful model for predicting interactions between quarks, leptons, and force carriers, with an accurate prediction for precision measurements, but has some faults such as, the Hierarchy problem, dark matter, and a Grand Unified Theory. We have seen that including SUSY can allow for possible solutions, such as: a dark matter candidate as the LSP, bosonic-fermionic loop corrections for the Higgs boson mass, and a unification of the fundamental forces at large energies. Then once investigating the theory of SUSY we were able to determine that the top squark could be the lightest squark, which allows us to develop multiple searches for this proposed theory.

2.4 Current SUSY Results

Here we see the most current results from searches for the top squark. These have been completed with data from the first part of Run 2 with 35.9 fb^{-1}. This analysis was completed with the most up-to-date identification methods for particles in the SM. From this Analysis, all 104 search region bins, as well as the corresponding single-lepton control region bins, the γ+jets control region bins and the QCD control regions, are fit simultaneously in order to evaluate the cross section excluded at 95% confidence level for each signal benchmark point.

The easiest way to think about the plots shown in 2.10, 2.11, 2.12, 2.13, 2.14, is that there is a calculated limit for each mass point. The x-axis is the possible mass range for the $\widetilde{t}$, $m_{\widetilde{t}}$ and the y-axis is the possible range for the $\tilde{\chi}_1^0$, $m_{\tilde{\chi}_1^0}$. Each point in this 2D space has a color representation for the value of the upper limit on the cross section at a confidence level of 95%.

With the comprehensive analysis that was performed in 2016, we have various limits on the multiple decay modes of the $\widetilde{t}$ which will be covered completely in Section 5. The comprehensive limits on the $\widetilde{t}$ mass range from values of 550 to 1.1 TeV for all of the all-hadronic decay modes. The CMS Collaboration has also

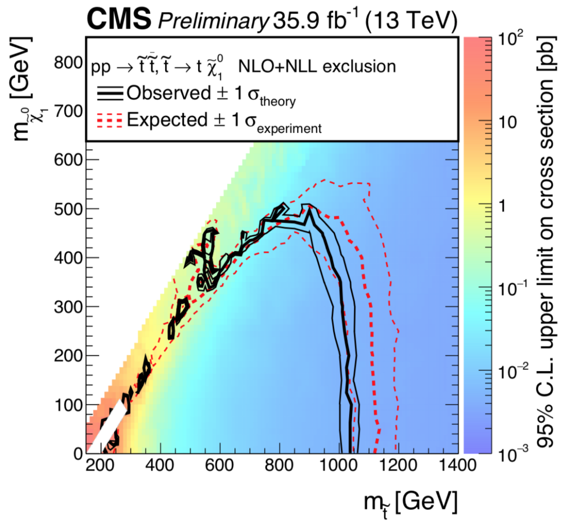

Figure 2.10 : Limits for the mass parameter space for T2tt decays. With a current limit of 1.1 TeV for a minimal neutralino mass.

combined the limits from the separate analyses which concentrate on the 1-lep, 2-lep, MT2, and HT missing analyses. The conbination of these has shown that we can set limits on the $\widetilde{t}$ mass range for masses of 800 to 1100 GeV.

From the Fig. 2.10, 2.11, 2.12, 2.13, 2.14, and 2.15, we know that we are able to exclude a large mass range for the $\widetilde{t}$ and $\tilde{\chi}_1^0$. Since this is one for a luminosity of 36.8 fb^{-1}, we can expect improved limits with all of the data from Run 2, which is 137 fb^{-1}. The new version of the analysis also has a redesigned search region to allow for more sensitive results, while also impoving various object definitions.

2.5 What are we looking for? And why?

As discussed in Sec. 2.1, the SM is a robust theory that is useful for describing the interations of visable matter in the universe. It has been through many robust test, while also able to make many predictions. Unfortunately, we have seen that a

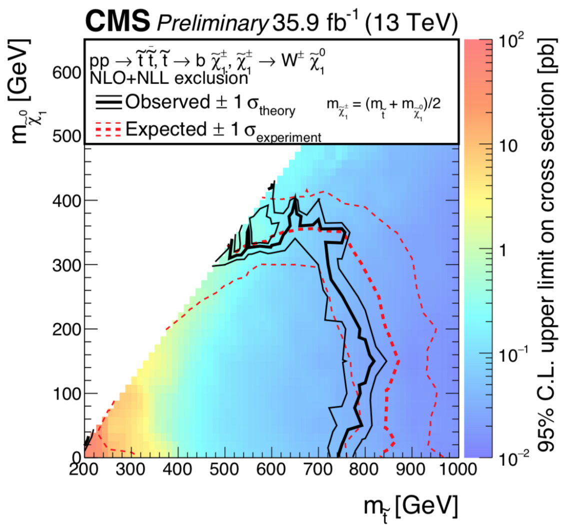

Figure 2.11 : Limits for the mass parameter space for T2bW decays. With a current limit of 750 GeV for a minimal neutralino mass.

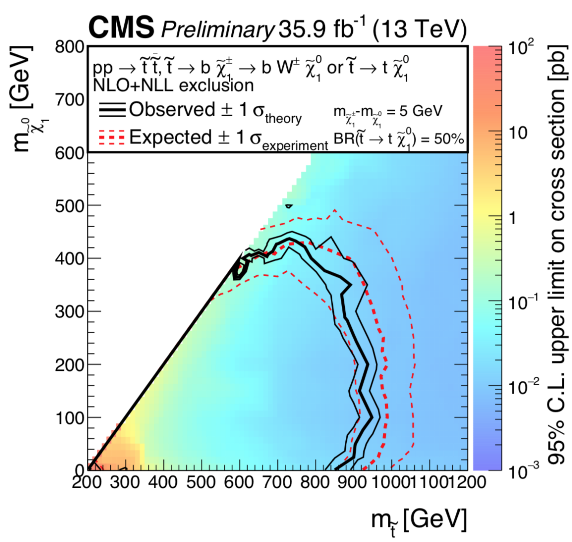

Figure 2.12 : Limits for the mass parameter space for T2tb decays. With a current limit of 850 GeV for a minimal neutralino mass.

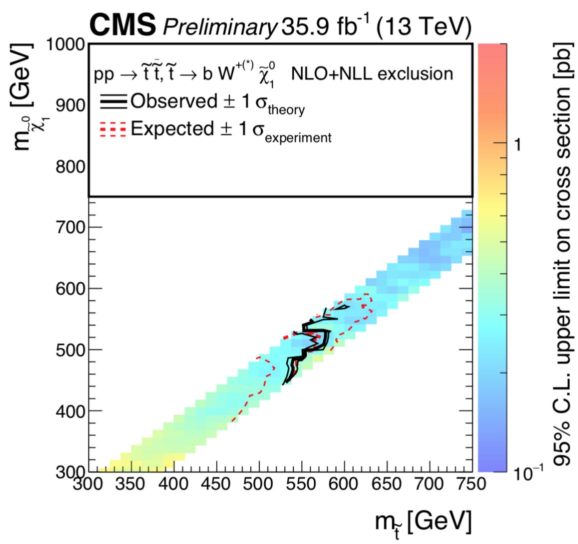

Figure 2.13 : Limits for the mass parameter space for T2fbd decays. Which has a range of 550 GeV for a $\tilde{\chi}_1^0$ mass of approx. 500 GeV.

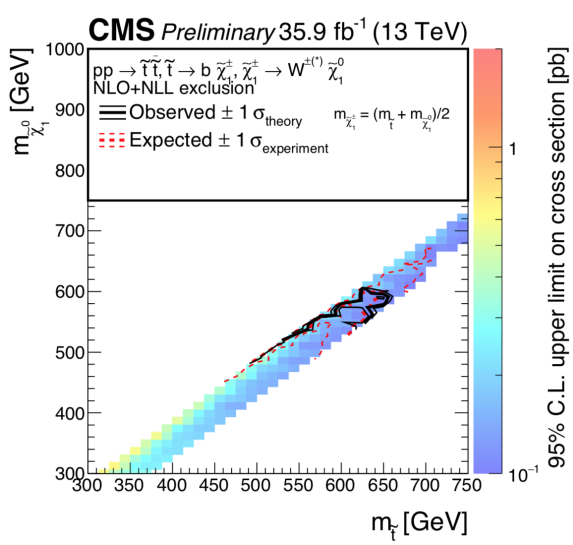

Figure 2.14 : Limits for the mass parameter space for T2bWC decays. Which has a range of 550 to 675 GeV for a $\tilde{\chi}_1^0$ mass of 600 GeV.

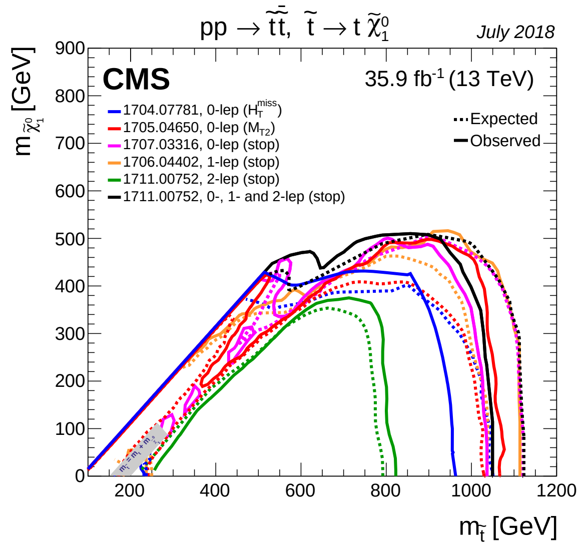

Figure 2.15 : Limits for the mass parameter space for T2tt decays using results from all the analysis in CMS. With a current limit of 800 GeV to 1.1 TeV for a minimal neutralino mass.

few unknowns such as, dark matter, the hierarchy problem, and a possible GUT, are currently unexplained. We then showed that a possible solution to these is SUSY, Sec. 2.3, provides a good dark matter condidate, LSP, allows for the convergence of the EM, Weak, and Strong force at large energy scales, and allows the higgs mass to be renormalizable without fine tuning.

From this, we have determined that the top squark is most likely to have the smallest squark mass in the MSSM. There has been many searches for the top squark decaying to many modes which are summarized in Fig. 2.15. As of right now we have set a limit on the $\widetilde{t}$ mass, $m_{\widetilde{t}} > 800$ GeV or $m_{\widetilde{t}} > 1100$ GeV depending on the analysis. Now we plan on using all of the data from Run2, 137 fb^{-1}, along with an improved search design to probe further into the mass parameter space of the $\widetilde{t}$ and $\tilde{\chi}_1^0$.

Chapter 3

Compact Muon Solenoid

3.1 The Detector

The Compact Muon Solenoid (CMS) is a particle detector as part of the Large Hadron Collider (LHC) which is located near Geneva, Switzerland as part of the CERN collaboration. The CMS detector is 21.6 m long, 15 m diameter, and 14,000 tons and is used to detect many different species of particles. It is separated into layers that, from the interaction vertex outward are, the silicon tracker, Electromagnetic Calorimeter (ECAL), Hadronic Calorimeter (HCAL), superconducting solenoid, and the muon chambers, see Fig. 3.1.

The CMS detector is designed to detect the decay products of most of the particles of the SM, except for neutrinos since they are weakly interacting and will almost certainly pass through the entire earth without an interaction. A defining feature of CMS is the 12.6-m long, 5.9 m inner diameter, 3.8 T superconducting solenoid. This is used to bend the trajectory of charged particles thoughout the detector, such that we can reconstruct the momentum and charge of the particles. The LHC provides a 13 TeV proton-proton beam (4.5 TeV heavy ion) beam with a bunch crossing every 25 ns (50 ns) to produce interaction at luminosities up to $2.5 \times 10^{34}\mathrm{cm}^{-2}s^{-1}$.

The coordinate system of CMS has the origin at the nominal collision point in the center of the detector. The y-axis points vertically upward, x-axis points radially inward toward the center of the LHC, and z-axis points along the beam directions

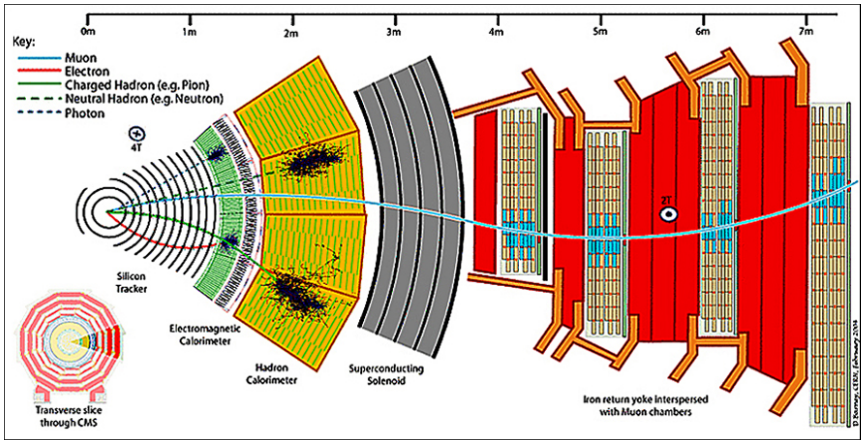

Figure 3.1 : A cross-section of the CMS detector, oriented by looking down the direction of the beam pipe.

towards the Jura mountains from LHC Point 5. The polar angle θ is measured from the z-axis and the azimuthal angle ϕ is measured in the $x-y$ plane from the x-axis. The pseudorapidity of a particle is defined as $\eta = -\ln\tan(\theta/2)$ where θ is the angle between the particle momentum and the positive direction of the beam axis, two notable values are $\eta = 0$ at $\theta = \pi/2$ and $\eta = \inf$ at $\theta = 0$. Pseudorapidity is quite useful since the difference of pseudorapidities is Lorentz invariant. The transverse components of momentum, p_T, and energy, E_T, are computed using the x and y components of the particles.

3.1.1 Tracker

The silicon tracker is made up of two different detectors, the silicon pixels and the silicon strip tracker. This is the inner most detector for CMS and receives the largest flux of particles during operation. This requires it to be radiation hard and operate with a fine granularity.

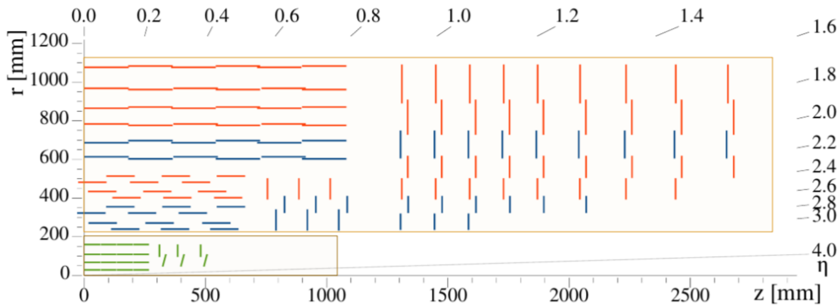

Figure 3.2 : Geometry of the CMS Tracker, the inner most region in green is the pixel detector while the outer region in blue and red are the silicon strips.

3.1.1.1 Pixel Detector

The pixel detector was recently upgraded during the winter of 2016/2017. It is approximately 1 m long with four barrel layers ranging from 3.0, 6.8, 10.2, and 16.0 cm from the beam axis and three endcap disks, see fig. 3.2. Since it is the closest detector to the interaction vertex it therefore has the highest particle flux at $10^7/\text{cm}^2/s$ at $r = 10$ cm. The resolution is 9.4 μm in $r - \phi$ and $20 - 45$ μm in z.

The pixel detector contains 1,184 modules in the barrel pixels (BPIX) and 672 modules in the forward pixels (FPIX). The number of individual pixels is 79 (45) million in the BPIX (FPIX) regions, respectively, with a pixel size of 100×150 μm^2. A pixel module contains two layers, a silicon layer that is bump bonded to 16 Readout Chips (ROCs) which form a module of 66560 pixels, see fig. 3.3. Each unit is controlled with one or more Token Bit Managers (TBMs) which controls the readout of the digital signal from the pixels to the Front-end Driver (FED). For BPIX Layers 3, 4 and all of FPIX there is 1 TBM per module. BPIX layer 2 has 2 TBMs with each one controlling 8 ROCs, while BPIX layer 1 has 4 TBMs with each one controlling 4 ROCs. The information from each module is split into two channels with each

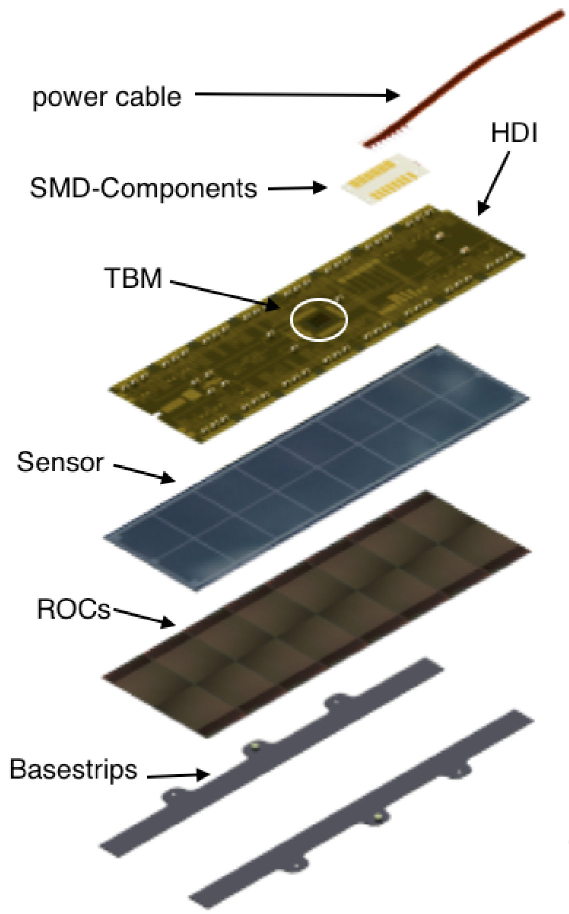

Figure 3.3 : Components of the pixel modules. Made up of a silicon layer, a grid of 8 ROCs which are attached via bump bonds. This is all controlled with a TBM connection to read out data.

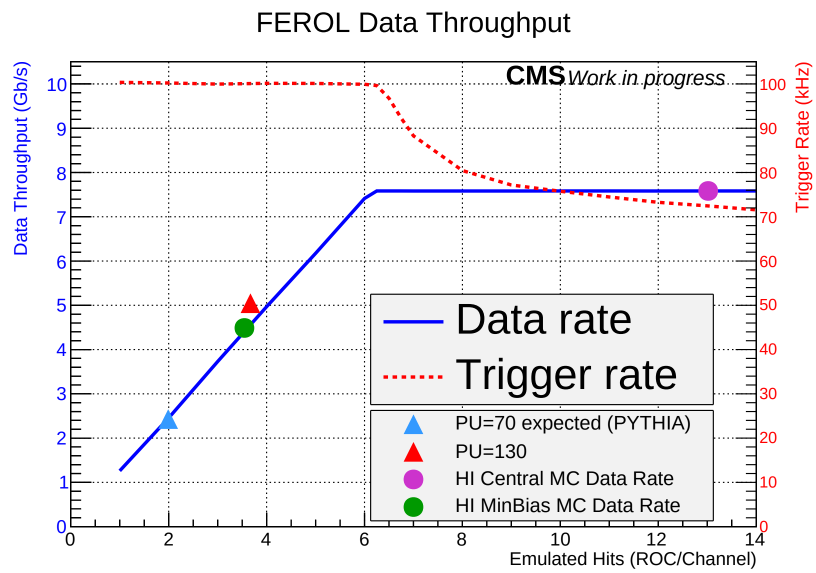

Figure 3.4 : Measuring the throughput of the FED with the emulated and simulated events provided by the FED Tester. The Data rate is shown as the solid blue line with the corresponding trigger rate as the dotted red line. The simulated event sizes are shown as their equivalent emulated hits/ROC/channel on the data line.

containing 8, 4, or 2 ROCs. These are encoded together by the TBM before being sent to the FED.

The silicon pixel system is set up as a reverse p-n junction, where the pixels are in the n-type region. As a charged particle travels through the silicon it creates electron-hole pairs. A voltage difference is applied to the silicon such that the electrons will deposit onto the pixels. Since the detector is inside of the magnetic field, a lorentz drift will cause the electrons to reach more than one pixel and increase the resolution. As the pixel system continues to be irradiated with large quantities of particles the voltage in the silicon decreases. This will lead to less charge sharing between the pixels and a decrease in resolution of particle locations.

The data, from the pixels, is sent via optical fiber to the FED where is decoded and processes the information. The FED is responsible for identifying the relevant data, determining possible error states, and packaging the information to be sent to the central Data Acquisition (cDAQ) of CMS. Each of the 108 FEDs, for the pixels, receives 24 independent fibers from the detector. Each of these fibers contains 2 channels from the pixel module. Through robust testing with the FED Tester [Cite here], we have confirmed that the FED is able to attain a maximum data throughput of approximately 7.5 Gbps, see fig. 3.4.

3.1.1.2 Silicon Strips

The silicon strips have a 200 m^2 active region with 15,148 modules that are distributed in 10 barrel layers and $9 + 3$ endcap disks. This has a cell size ranging from 10 cm $\times$ 80 μm to 25 cm $\times$ 180 μm since the particle flux decreases further away from the vertex, Fig. 3.5. It has a resolution of $23 - 24$ μm in $r - \phi$ and 23 μm in z for the microstrip tracker.

There are two types of silicon strip module, see Fig. 3.5, which are in the layour shown in Fig. 3.2. The orange modules are single sided reverse p-n silicon sensors, while the blue modules are double sided by having two single modules mounted back-to-back at a 100 mrad angle. This improves the 3D tracking, but unlike the pixel detector this is an analog readout system.

3.1.2 Electromagnetic Calorimeter

The ECAL is a homogeneous calorimeter made out of 61,200 lead tungstate ($PbWO_4$) crystals in the barrel and 7,324 crystals in each endcap. The barrel region has an inner radius of 129 cm and covers a pseudorapidity range of $0 < |\eta| < 1.479$. The encaps are 314 cm from the interaction point and cover a range $1.479 < |\eta| < 3.0$

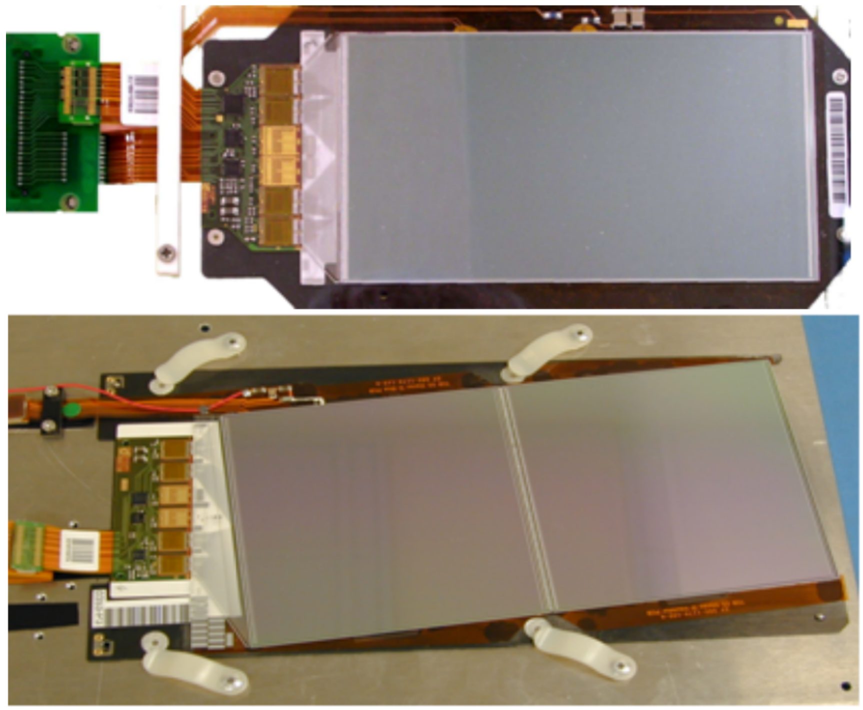

Figure 3.5 : The top module is a single sided reverse p-n silicon sensor. The bottom is two silicon sensors mounted back-to-back at a 100 mrad angle.

in pseudorapidity. Lead tungstate was chosen for the crystals since it has a short radiation length, $X_0 = 0.89$ cm , fast with 80% of the light being emitted within 25 ns, and it's radiation hard. Each crystal in the barrel has a cross-section of $\approx 22 \times 22$ mm^2 and length of 230 mm, while the endcap crystals are 28.6×28.6 mm^2 and length of 220 mm corresponding to $25.8X_0$ and $24.7X_0$, respectively. An ECAL uses electromagnetic showers to detect particles that interact electromagnetically. Electrons traveling through the material will radiate a photon via bremsstrahlung then the photon will pair produce two electrons. Combining these two processes leads to electromagnetic showers as the particles travel through the detector. The process will continue until a critical energy is reached such that an electron cannot radiate any further and will then lose energy via collisions. The hadrons that are created in the collisions will also interact in this way, but because of their large mass the penetrate through the entire ECAL. The resulting light is recorded by silicon avalanche photodiode (vaccuum phototriodes) in the barrel (endcap).

3.1.3 Hadronic Calorimeter

The HCAL is a hermetic calorimeter consisting of alternating layers of brass as the absorber material and a scintillator. Brass is chosen since it is non-magnetic and has a relatively short interaction length. In the scintillator, a portion of the energy from the hadron in converted into visible light which is then measured by a hybrid photodiode tube to measure the energy. The barrel part of the HCAL consists of 2304 towers that are segmented into $\Delta\eta \times \Delta\phi = 0.087 \times 0.087$ pieces that cover a region $0 < |\eta| < 1.4$ in pseudorapidity. The encap region consists of 2304 towers with varying segmentation sizes and a coverage of $1.3 < |\eta| < 3.0$.

There are two additional parts of the HCAL to allow for maximum coverage of the detector volume. There is a outer hadron detector that is located outside the superconducting solenoid, which covers a slightly smaller pseudorapidity range as the barrel region. They serve as a tail catcher for hadron showers that penetrate all the way through the inner HCAL and solenoid. A forward hadron calorimeter, located 11.2 m from the interaction point covering a pseudorapidity $3.0 < \eta < 5.0$, made out of steel/quartz fiber is specifically designed for the columnated Cerenkov light in this region.

3.1.4 Superconducting solenoid

Surrounding most of this is the superconducting solenoid which is 12.6 m long with a 5.9 m radius. The field strength is 3.8 T which has a stored energy of approximately 2.7 GJ. The magnet is designed such that a muon with momentum, $p = 1$ TeV, will have a momentum resolution of $\Delta p/p \approx 10\%$. The solenoid is a high-purity aluminium-stabilized conductor, which is a similar material used in other large solenoids.

3.1.5 Muon Chambers

The muon system has three main detection systems that are used to identify a muon candidate. In the barrel region, drift tube (DT) chambers are used since the neutron background, muon rate, and magnetic field are all small. In the endcaps, cathode strip chambers (CSCs) are used since the relative values stated before are much larger. The neutron background is largely radially dependent so the CSCs will recieve a larger flux, while the muon rate is dominated by low p_T muons which will interact in the endcap regions. Included throughout the whole system are resistive plate chambers (RPC).

The DT consists on 250 chambers in 4 barrel layers at a radii of 4.0, 4.9, 5.9, and 7.0 m from the beam axis. A DT chamber is an array of anode wires in a gaseous medium where the walls are cathodes. A muon passing through the gas will ionize some atoms which are then forced towards the anode wires by the electric field. The drift time of the electrons can then be calculated to within a couple of ns such that a good spatial resolution is achieved. The maximum designed drift length is 2.0 cm. Each station of the DT will give muon vector for each candidate with a ϕ precision of 100 μm in postion and 1 mrad in direction.

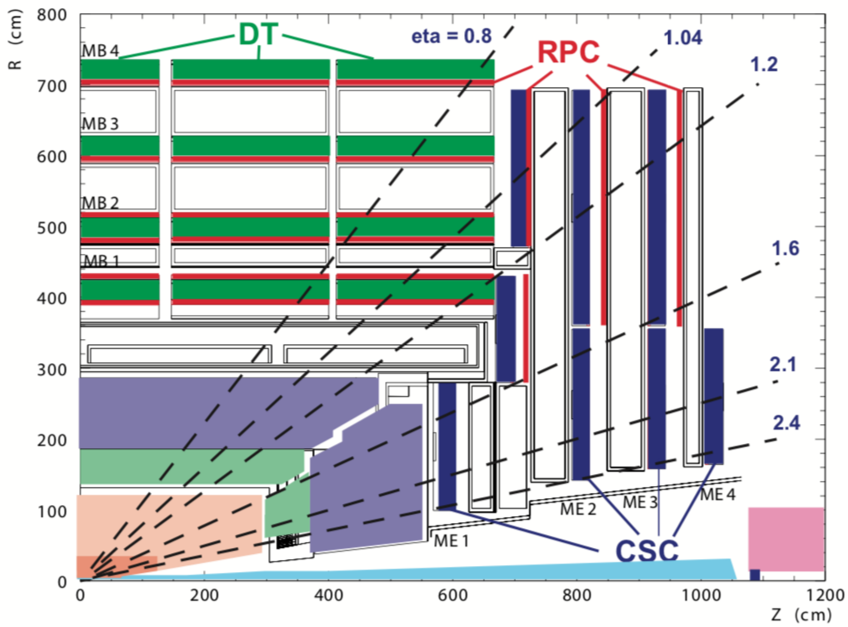

Figure 3.6 : A quarter cross-section of the three muon detection systems for CMS.

The CSC system uses the same concept as the DT system, but also includes a measurement of the ions that follow the electric field to the cathode strips. In this system the anode wires and the cathode strips are perpendicular so the collected charge on both provide a accurate position measurement. The RPC system contains two parallel plates, anode and cathode, the charge is measured by external metallic strips that can quickly measure the momentum of a muon and decide if the event should be triggered.

3.2 Detector Methods

Using the objects and information from each of the subdetectors we can measure the important information required for doing innovative physics analysis, such as, the $\widetilde{t}$ search. Since the search is dependent on large missing energies it is dependent on measuring all forms of energy in the standard model and checking for any inefficiencies. The CMS detector is designed to be an all encompassing detector to measure multiple processes in the SM and beyond.

Chapter 4

Search Strategy

4.1 Physics Objects

There are many different types of physics objects that we are interested in when working with particle physics experiments. Since the particles that we are interested in have very short lifetimes, $\mathcal{O}(\text{decay}) = 10^{-23}$ s, we mainly interact with the decay products of the event, such as, jets (N_j), heavy object tagging (N_t, N_W, N_{res}), missing transverse momentum ($\not{E}_T$), sum scalar jet momentum (H_T), number of secondary vertices (N_{SV}), transverse momentum of leading b jet (p_T^b), transverse mass between tagged b quarks amd $\not{E}_T$ ($m_T(b_{1,2}, \not{E}_T)$), Initial State Radiation, and lepton identification.

4.1.1 Jets

In an interaction whenever a quark is made it must come in pairs ($q\bar{q}$) such that the total color and electric charge of the interaction is neutral. Typically due to conservation of momentum the quarks may originally be produced near the interaction point but will quickly start to move away from each other. Eventually the quarks will move far enough apart and will have enough potential energy in the gluon connections between them that it is now more efficient to create a new quark-antiquark ($q\bar{q}$) pair. This will continue to occur in a sequence of radiating gluons and producing new pairs of charged particles. In the final state, the energy deposited in the HCAL is due

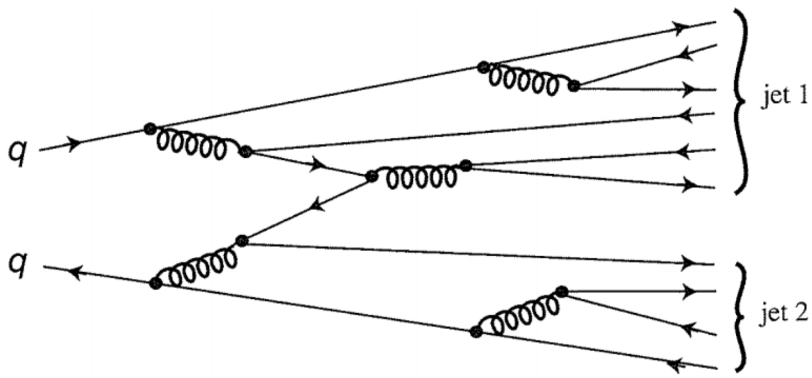

Figure 4.1 : A diagram of a quark pair radiating gluons that decay into more quark pairs in a process called hadronization [8].

to a cluster of charged particles of a certain radius, $\Delta R = \sqrt{\Delta\eta^2 + \Delta\phi^2}$. There are many algorithms to reconstruct the jets, we are mainly interested in the anti-kT Jet algorithm [5] method which uses the transverse momentum of the particles within a certain radius $\Delta R = 0.4(0.8)$ for AK4(AK8) jets [6, 7]. Once the jets have been identified, we cause analyse their respective properties to determine the likelihood of the particle it originated from, such as a $b, t,$ or W.

4.1.2 Heavy Object Tagging

Since this search is looking for a massive particle which then decays to slightly less massive particles we need to be able to identify and distinguish between them. We use various algorithms and neural networks to identify jets from b quarks, $b-$jets or from t quarks.

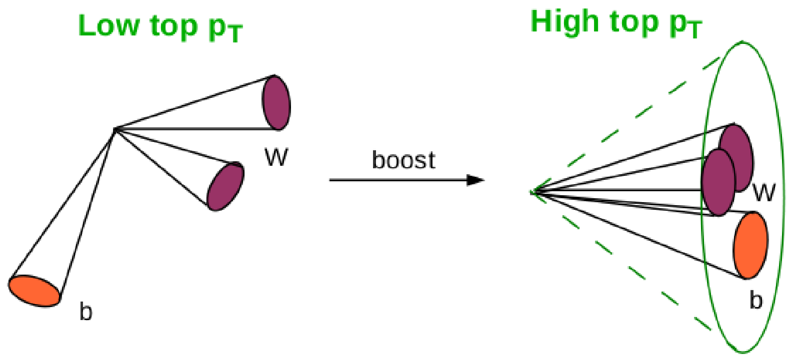

Figure 4.2 : The two types of top quark reconstuctions, when each decay product is easily identifiable (resolved) or when the particles are close together (boosted).

4.1.2.1 B-Tagging

Firstly, b-tagged jets which are jets that are likely to have originated from a b quark. These are identified reconstructing where the jet originated from and comparing the distance away from the interaction point. A b quark is a relatively long-lived particle and can travel many millimeters before decaying. Since we have a resolution of μm this is not a problem. For b quarks with large transverse momentum, we use a Deep Combined Secondary Vertex (DeepCSV) algorithm that involves neural networks.

$b-$ jets are identified using the Run 2 version of the Deep Combined Secondary Vertex (DeepCSV) algorithm. The medium working point recommended by the B-tag POG, corresponding to a threshold of 0.6324m 0.4941, and 0.4184 for the 2016, 2017, and 2018 respectively [9–11].

4.1.2.2 Top/W Tagging

The anti-kt algorithm using a distance parameter, $\Delta R = 0.8$, is expected to contain the energy clusters of all of the decay product of boosted t quarks, see Fig. 4.2, with $p_T > 300$ GeVor Wbosons with $p_T > 200$ GeV. The requirements are:

- Medium working point $> 0.937, 0.895, 0.895(0.973, 0.991, 0.991)$ for boosted t (W) for the separate 2016, 2017, and 2018 eras, respectively.
- Reconstructed soft drop mass: $105 < m_t < 210$ GeV and $65 < m_W < 105$ GeV.
- Boosted tops: $p_T = 300$ GeV, $|\eta| < 2.0$ and W: $p_T = 200$ GeV, $|\eta| < 2.0$

There is another type of top that can be reconstructed, which is when each subjet of the top decay can be resolved into each individual jet, denoted as a resolved top, see Fig. 4.2. The requirements are:

- Medium working point: 0.92 for all eras.
- $|\eta(j_{1,2,3})| < 2.4$ and b-tag desciminator: $> 0.6324, 0.4941, 0.4184$ for the separate 2016, 2017, and 2018 eras, respectively. The number of jets that pass these cuts should be ≥ 2.

These object definition are orthogonal to each other and are used to bin our search and control regions.

4.1.3 Missing Transverse Momentum

The missing transverse momentum is the negative vector sum of the total transverse momentum measured in the detector,

$$\not{E}_T = -\sum_{i \in \text{vis}} \overrightarrow{p}_{i,T}, \tag{4.1}$$

where the momentum runs over every visible(vis) particle in the event. Ideally, if the detector was 100% this quantity would always be zero due to conservation of momentum, but many things, such as detector efficiency, paticles that are weakly interacting, or particles beyond the SM will cause the missing energy. Because of these, this object is a good discriminator for searching for physics beyond the SM.

4.1.4 MET Filters

Need to add MET Filters here.

4.1.5 H_T

Another interesting quantity is H_T, which is the scalar sum of the $p_T$of all of the jets in an event,

$$H_T = \sum_{i \in \text{jets}} p_{i,T}. \tag{4.2}$$

This quantity is quite useful when trying to identify massive particles and is quite good at suppressing QCD multijet background.

4.1.6 Soft b-Tagging

The ability to identify secondary vertices is essential in searches for the top squark, see Sec. 5.1. Since the b quark is a long lived particle, about 10^{-12} seconds, that will travel many millimeters before decaying into other particles. The displaced vertex of the long lived b quark is reconstructed from the tracks that it produces in the detector. We then reconstruct the tracks to a point that is displaced from the primary vertex (PV) it is known as a secondary vertex (SV) and has the potential to be an long lived particle.

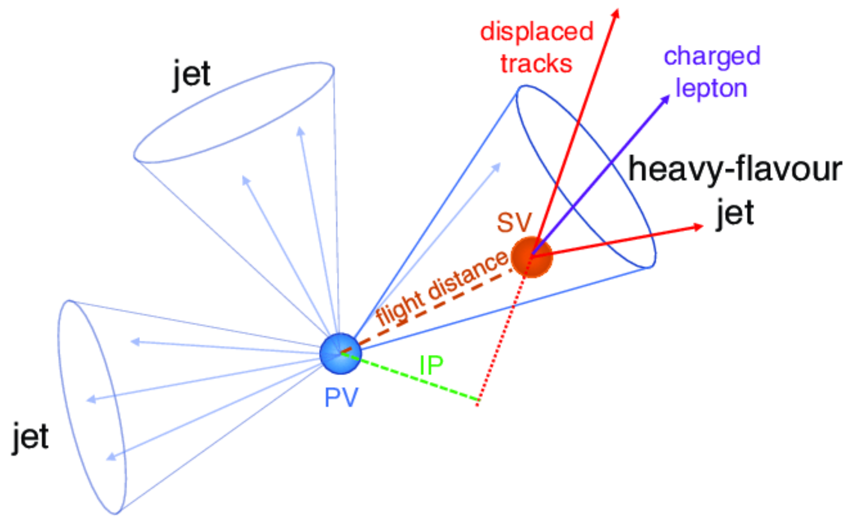

Figure 4.3 : A interaction that produces a long lived particle that has a reconstruced SV.

This search targets also models that produce very soft bottom or charm quarks. A large fraction of events contain b quarks with p_T below the 20 GeV jet p_T threshold which may thus fail to be reconstructed as jets or become b-tagged. Identification of these soft quarks improves our ability to separate potential signal events from the SM background. We therefore aim to identify b/c quarks based on the presence of a SV reconstructed using the Inclusive Vertex Finder (IVF) [12]. Additional requirements on SV observables are applied to suppress the background originating from light quarks. These selected SV may be referred to as soft b-tags and are constructed to be orthogonal to the jets and b-tagged jet used in this analysis.

The requirements on each SV to pass the soft b-tagging definition are:

- The distance in the transverse plane between the SV and the PV ≤ 3 cm.
- The significance of the distance, SIP3D, between the SV and thePV ≥ 4.

- The pointing angle, defined as $cos(\overrightarrow{PV,SV}, \overrightarrow{p}_{SV}) \geq 0.98$, where $\overrightarrow{p}_{SV}$ is the total four-momentum of the tracks associated to the SV.
- The number of tracks associated to the SV is greater or equal to 3.
- The p_T of the SV is less than 20 GeV.

4.1.7 Initial-state Radiation

Initial-state radiation (ISR) may be clustered into one of the large-R jets clustered with a distance parameter, $\Delta R = 0.8$. We use the larger radius jets to be sensitive to ISR with gluon splitting, when a jet radiates a qluon that pair produces two quarks. The ISR jet is identified as being the hardest of the large-R jets with $p_T > 200$ GeV which fails the loose b-tagging working point and is not identified as a top or W.

4.1.8 Lepton Identification

There are two sets of selection criteria used in the analysis for electrons and muons. A set of veto criteria are used to efficiently reject events with an isolated electron of muon in the search region, while more stringent requirements are imposed in some control regions that require high purity samples of isolated leptons.

Electron candidates are identified via a set of selection criteria established by the EGamma POG based on "Spring16" simulated samples in the 25ns bunch spacing scenario. The corresponding thresholds imposed on relevant variables are summarized in Table 4.1. The "Veto" working point is used to keep events with electrons out of the final search region. The "Medium" working point is used for the selection of leptonic control regions.

The loose muon definition recommended by the Muon POG is used for the purposes of the muon veto. A loose muon is identified as a PF muon and can be either a

	Veto Working Point		Medium Working Point	
	Barrel	Endcap	Barrel	Endcap
$\sigma_{i\eta i\eta}(\text{full5} \times 5) <$	0.0114	0.0352	0.0101	0.0283
$\lvert\Delta\eta_{\text{in}}\rvert <$	0.0152	0.0113	0.0103	0.00733
$\lvert\Delta\phi_{\text{in}}\rvert <$	0.216	0.237	0.0336	0.114
$\frac{h}{E} <$	0.181	0.116	0.0876	0.0678
$\frac{1}{E} - \frac{1}{p} <$	0.207	0.174	0.0174	0.0898
$\lvert d_0\rvert <$	0.0564	0.222	0.0118	0.0739
$\lvert d_z\rvert <$	0.472	0.921	0.373	0.602
N(expected missing inner hits) $\leq$	2	3	2	1
Conversion veto	pass	pass	pass	pass

Table 4.1 : Electron identification requirements, defined separately for electrons in the ECAL barrel and endcap regions. The tabulated numbers for each working point are the thresholds applied to the corresponding quantities in the first column. THESE NUMBERS NEED TO BE UPDATED!!!

global muon or an arbitrated tracker muon. Only candidates with transverse (longitudinal) impact parameter $|d_0| < 0.2$ cm ($|d_z| < 0.5$cm,) with respect to the primary vertex, are considered. The muon selection in leptonic control regions relies on the medium working point defined by the Muon POG for higher purity. The medium muon requirements are summarized in Table 4.2. They are applied in addition to the loose muon requirements. Selected muons are required to have transverse (longitudinal) impact parameters $|d_0| < 0.05$ cm ($|d_z| < 0.1$cm), with respect to the primary vertex.

Electrons and muons are considered to fulfill the veto isolation criteria if their mini-isolation is less than 0.1 or 0.2 respectrively, relative to the lepton p_T. The same thresholds are applied on the relative mini-isolation for electrons and muons in control samples.

Loose muon selection	yes
Fraction of valid tracker hits	> 0.8
In addition, either of the following sets of requirements:	
Global muon	yes
Normalized global-track χ^2	< 3
Tracker-Standalone position match	< 12
Track kink finder	< 20
Segment compatibility	> 0.303
OR	
Segment compatibility	> 0.451

Table 4.2 : The requirements for a particle trajectory to be tagged as a muon. THESE NUMBERS NEED TO BE UPDATED!!!

4.1.9 Tau Identification

The Tau ID has been studied extensively. After multiple studies which looked into the custum MVA [13, 14] similar to the one used in Ref. [15], the cut-based IsoTrack method, and Tau POG MVA method of Identifying Taus. The methods which provide the best improvement to the efficiency of identifying taus with a small fake rate is the combination of IsoTrack and Tau POG MVA. With the inclusion of the combined method for identifying hadronically decaying taus, the veto percentage is $\approx 29.0\%(7.2\%)$ with a efficiency of the veto efficiency of $\approx 49.1\%(22.6\%)$ for SM background (signal), see Appendix. BLANK.

4.2 Search Strategy

4.2.1 Trigger

The following filters, recommended by the JetMET POG, are applied to 2016, 2017, and 2018 eras:

- goodVertices
- HBHENoiseFilter
- HBHENoiseIsoFilter
- EcalDeadCellTriggerPrimitiveFilter
- BadPFMuonFilter
- GlobalSuperTightHalo2016Filter
- eeBadScFilter

There is an addition ecalBadCalibFilter for 2017 and 2018 eras only.

4.2.2 Baseline Selection

Following the same methods as above, we have a loose pre-selection which is refered to as the baseline selection. This will place a selection on jets and $\not{E}_T$which is used to eliminate a large fraction of background events. We define the baseline selection as:

- $N_{e,(\mu)} = 0, (p_T > 5$ GeV, $|\eta| < 2.5(2.4), \text{miniISO} < 0.1(0.2))$
- $N_{isoTrk} = 0, (p_T > 5(10)$ GeV, ISO $< 0.2(0.1)$ for electron/muons(pions))
- $N_{tauPOG} = 0, (p_T > 20$ GeV, $|\eta| < 2.4)$, medium working point
- $N_j \geq 2, (p_T > 20$ GeV, $|\eta| < 2.4)$
- $\not{E}_T > 250$ GeV, to reach the plateau of the trigger efficiency
- $H_T > 300$ GeV

- HEM Veto for part of 2018 data: $-3 \leq \eta \leq -1.4, -1.57 \leq \phi \leq -0.87$

In Addition to this, we allow for two separte sets of additional selections to apply to the low and high Δm search regions to further reduce background. The high Δm baseline selection includes the baseline selection and additionally,

- $N_j \geq 5, (p_T > 20$ GeV, $|\eta| < 2.4)$
- $N_b \geq 1, (p_T > 20$ GeV, $|\eta| < 2.4)$, medium DeepCSV
- $\mathrm{Min}[|\Delta\phi(\not{E}_T, j_1)|, |\Delta\phi(\not{E}_T, j_2)|, |\Delta\phi(\not{E}_T, j_3)|, |\Delta\phi(\not{E}_T, j_4)|] \equiv \Delta\phi_{1234} > 0.5$, where j_1, j_2, j_3, j_4 are the four leading jets in p_T. This requirement is to reduce the QCD multijet background.

Next, the low Δm baseline selection has the following addition selections,

- $N_t = 0, N_W = 0, N_{res} = 0$, where N_t and N_W are the number of merged tops and W's, respectively, and N_{res} is the number of resolved tops
- An ISR jet is defined in Sec. 4.1.7 with $p_T(ISR) > 200$ GeV, $|\eta| < 2.4, |\Delta\phi(j_{ISR}, \not{E}_T)| > 2$.
- $\not{E}_T/\sqrt{H_T} \equiv S_{\not{E}_T} > 10$, where H_T is calculated as the scalar sum of the $p_T$of jets with $p_T > 20$ GeV and $|\eta| < 2.4$.
- $|\Delta\phi(\not{E}_T, j_1)| > 0.5, |\Delta\phi(\not{E}_T, j_{2,3})| > 0.15$, where j_1, j_2, j_3 are the three leading jets in p_T.

4.3 Search Regions

Table 4.3 : Summary of the 151 disjoint search regions that mainly target high Δm signal models. The high Δm baseline selection is again $N_j \geq 5$, $\not{E}_T > 250\ GeV$, $N_b \geq 1$, and $\Delta\phi_{1234} > 0.5$.

$M_T(b_{1,2}, \not{E}_T) < 175\,\mathrm{GeV}$						
N_j	N_b	N_t	N_W	N_{res}	H_T [GeV]	$\not{E}_T$ [GeV]
≥ 7	$1, \geq 2$	≥ 0	≥ 0	≥ 1	≥ 300	$250-300,\ 300-400,\ 400-500,\ \geq 500$
$M_T(b_{1,2}, \not{E}_T) \geq 175\,\mathrm{GeV}$						
N_j	N_b	N_t	N_W	N_{res}	H_T [GeV]	$\not{E}_T$ [GeV]
≥ 5	$1, \geq 2$	0	0	0	≥ 1000	$250-350,\ 350-450,\ 450-550,\ \geq 550$
≥ 5	1	≥ 1	0	0	$300-1000,\ 1000-1500,\ \geq 1500$	$250-550,\ 550-650,\ \geq 650$
		0	≥ 1	0	$300-1300,\ \geq 1300$	$250-350,\ 350-450,\ \geq 450$
		0	0	≥ 1	$300-1000,\ 1000-1500,\ \geq 1500$	$250-350,\ 350-450,\ 450-550,\ 550-650,\ \geq 650$
		≥ 1	≥ 1	0	≥ 300	$250-550,\ \geq 550$
		≥ 1	0	≥ 1	≥ 300	$250-550,\ \geq 550$
		0	≥ 1	≥ 1	≥ 300	$250-550,\ \geq 550$
≥ 5	2	1	0	0	$300-1000,\ 1000-1500,\ \geq 1500$	$250-550,\ 550-650,\ \geq 650$
		0	1	0	$300-1300,\ \geq 1300$	$250-350,\ 350-450,\ \geq 450$
		0	0	1	$300-1000,\ 1000-1500,\ \geq 1500$	$250-350,\ 350-450,\ 450-550,\ 550-650,\ \geq 650$
		1	1	0	≥ 300	$250-550,\ \geq 550$
		1	0	1	$300-1300,\ \geq 1300$	$250-350,\ 350-450,\ \geq 450$
		0	1	1	≥ 300	$250-550,\ \geq 550$
		2	0	0	$300-1300,\ \geq 1300$	$250-450,\ 450-650,\ \geq 650$
		0	2	0	≥ 300	≥ 250
		0	0	2	$300-1300,\ \geq 1300$	$250-450,\ 450-650,\ \geq 650$
		$N_t + N_W + N_{res} \geq 3$			$300-1300,\ \geq 1300$	$250-450,\ \geq 450$
≥ 5	≥ 3	1	0	0	$300-1000,\ 1000-1500,\ \geq 1500$	$250-350,\ 350-550,\ \geq 550$
		0	1	0	≥ 300	$250-350,\ 350-550,\ \geq 550$
		0	0	1	$300-1000,\ 1000-1500,\ \geq 1500$	$250-350,\ 350-550,\ \geq 550$
		1	1	0	≥ 300	$250-550,\ \geq 550$
		1	0	1	$300-1300,\ \geq 1300$	$250-350,\ 350-550,\ \geq 550$
		0	1	1	≥ 300	$250-550,\ \geq 550$
		2	0	0	$300-1300,\ \geq 1300$	$250-550,\ \geq 550$
		0	2	0	≥ 300	≥ 250
		0	0	2	$300-1300,\ \geq 1300$	$250-550,\ \geq 550$
		$N_t + N_W + N_{res} \geq 3$			≥ 300	$250-450,\ \geq 450$

Table 4.4 : Summary of the 53 disjoint search regions that mainly target low Δm signal models. The low Δm baseline selection is again $N_j \geq 2$, $\not{E}_T > 250\ GeV$, $N_t = N_W = N_{res} = 0$, $N_b \geq 0$, $M_T(b_{1,2}, \not{E}_T) < 175\ GeV$ (when applicable), $|\Delta\phi(\mathrm{j}_1, \not{E}_T)| > 0.5$, $|\Delta\phi(\mathrm{j}_{2,3}, \not{E}_T)| > 0.15$, $p_T(ISR) > 200$ GeV, $|\eta(ISR)| < 2.4$, $|\Delta\phi(j_{\mathrm{ISR}}, \not{E}_T)| > 2$, and $S_{\not{E}_T} > 10$.

N_j	N_b	N_{SV}	$p_T(ISR)$ [GeV]	$p_T(b)$ [GeV]	$\not{E}_T$ [GeV]
$2-5$	0	0	> 500	-	$450-550$, $550-650$, $650-750$, > 750
≥ 6		0			$450-550$, $550-650$, $650-750$, > 750
$2-5$		≥ 1			$450-550$, $550-650$, $650-750$, > 750
≥ 6		≥ 1			$450-550$, $550-650$, $650-750$, > 750
≥ 2	1	0	$300-500$	$20-40$	$300-400$, $400-500$, $500-600$, > 600
		0	$300-500$	$40-70$	$300-400$, $400-500$, $500-600$, > 600
		0	> 500	$20-40$	$450-550$, $550-650$, $650-750$, > 750
		0	> 500	$40-70$	$450-550$, $550-650$, $650-750$, > 750
		≥ 1	> 300	$20-40$	$300-400$, $400-500$, > 500
≥ 2	≥ 2	≥ 0	$300-500$	$40-80$	$300-400$, $400-500$, > 500
≥ 2			$300-500$	$80-140$	$300-400$, $400-500$, > 500
≥ 7			$300-500$	> 140	$300-400$, $400-500$, > 500
≥ 2			> 500	$40-80$	$450-550$, $550-650$, > 650
≥ 2			> 500	$80-140$	$450-550$, $550-650$, > 650
≥ 7			> 300	> 140	$450-550$, $550-650$, > 650

Chapter 5

Stop quark Production and Backgrounds

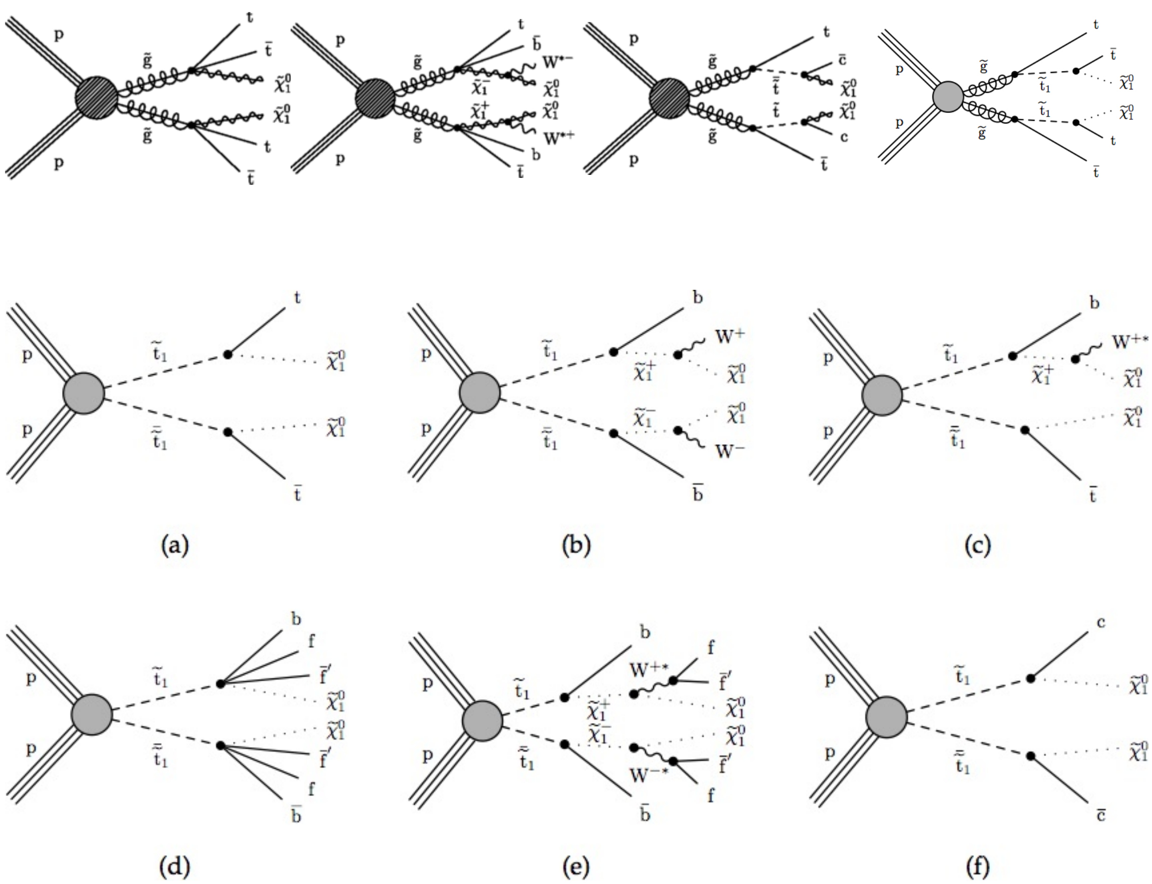

5.1 Production and Decay Modes

Gluon fusion.

Main decay mode mode $\widetilde{t} \to t + \tilde{\chi}_1^0$, $\widetilde{t} \to b + \tilde{\chi}^+$. The top quark most likely decays into a b quark and W boson.

5.2 Standard Model Background

Signal events can be mimicked by SM events that have a large number of jets and missing energy.

Broken up into four major backgrounds, Lost Lepton (LL), Znunu, QCD, Rare decays

5.2.1 Lost Lepton

The contribution from the $t\bar{t}$ and W+jets processes arises from leptonic decays of the Wboson where the charged lepton is outside the kinematic acceptance of CMS or evades identificaiton by the dedicated lepton vetoes. Large $\not{E}_T$can be generated by the associated neutrino and the lepton that is not reconstructed, allowing such events to enter the search regions. This background is collectively referred to as the "Lost Lepton" (LL) background. Contributions arising from ttW and single-top processes also enter into this category, but with much smaller importance.

Studies in simulation indicate that the event kinematics for different lepton flavors are similar enough to allow us to estimate them collectively from a single control sample in data that has event characteristics similar to those of the search sample. Because of this, we use the single-lepton control sample to estimate the LL background, using the method descrived in detail in Ref. [18]. The single-lepton sample consists of events that have one lepton satisfying the lepton-veto criteria. In order to suppress potential signal contamination, we require $M_T(l, \not{E}_T) < 100 GeV$. If there is more than one selected lepton, we randomly select which lepton is chosen to determine the $M_T(l, \not{E}_T)$. The requirement of low $M_T(l, \not{E}_T)$ also ensures orthogonality to the search regions used in the search for direct top squark production in the single-lepton final state, making it possible to statistically combine the results of the two searches. The selection applied to the single-lepton control sample follows the same selection on the search variables as in the zero-lepton selection with the exception of classification according to the number of top and W-tagged candidates.

5.2.1.1 Transfer Factors

The LL estimation in each search region is based upon the event count in data in the corresponding control region in the single-lepton sample. The count is extrapolated to the search region to obtain a prediction by means of a transfer factor obtained from simulation samples as follows:

$$N^{LL}_{pred} = TF_{LL} \cdot N_{data}(1l). \tag{5.1}$$

We want to suppress signal contamination by requiring $M_T(l, \not{E}_T) < 100$ GeV. This requirement confirms that it is orthogonal to the search reagions that are used in the search for direct top squark production in the single-lepton final state. Letting the two anaysis statistically combine the results in the future.

This allows us to have the same selection for the single-lepton control sample and the zero-lepton sample. The only exception is the number of top and W-tagged candidates? what is the difference betweeen a candidate and a particle?

The LL estimation is dependent on the yield of data in the corresponding CR and the TF calculated by the single-lepton sample. The transfer factor is defined as,

$$TF_{LL} = \frac{N_{MC}(0l)}{N_{MC}(1l)}, \tag{5.2}$$

where $N_{MC}(1l)$ is the event count observed in the corresponding CR and $N_{MC}(0l)$ use the event count in the corresponding SR.

Search region	$\not{E}_T$	singlelep	TF	pred
low Δm, $N_b = 0$, $N_{SV} = 0$, $p_T(ISR) > 500\,\mathrm{GeV}$, $2 \leq N_j \leq 5$				
0	450−550	7691	0.511±0.004	3932.19±52.90
1	550−650	3571	0.589±0.004	2101.77±38.32
2	650−750	1405	0.589±0.004	827.70±22.93
3	≥ 750	963	0.591±0.005	568.81±18.93
low Δm, $N_b = 0$, $N_{SV} = 0$, $p_T(ISR) > 500\,\mathrm{GeV}$, $N_j \geq 6$				
4	450−550	1411	0.414±0.005	584.63±16.85
5	550−650	735	0.424±0.006	311.72±12.26
6	650−750	328	0.409±0.008	134.20±7.81
7	≥ 750	334	0.400±0.007	133.56±7.71
low Δm, $N_b = 0$, $N_{SV} \geq 1$, $p_T(ISR) > 500\,\mathrm{GeV}$, $2 \leq N_j \leq 5$				
8	450−550	422	0.558±0.016	235.43±13.27
9	550−650	190	0.637±0.018	121.07±9.45
10	650−750	79	0.640±0.018	50.59±5.87
11	≥ 750	54	0.624±0.019	33.70±4.69
low Δm, $N_b = 0$, $N_{SV} \geq 1$, $p_T(ISR) > 500\,\mathrm{GeV}$, $N_j \geq 6$				
12	450−550	113	0.459±0.019	51.90±5.35
13	550−650	58	0.457±0.026	26.50±3.78
14	650−750	25	0.483±0.034	12.07±2.56
15	≥ 750	17	0.377±0.025	6.41±1.61
low Δm, $N_b = 1$, $N_{SV} = 0$, $M_T(b_{1,2}, \not{E}_T) < 175$ GeV, $300 < p_T(ISR) < 500\,\mathrm{GeV}$, $p_T(b) < 40\,\mathrm{GeV}$				
16	300−400	3082	0.843±0.014	2598.67±63.47
17	400−500	516	0.896±0.030	462.38±25.65
18	500−600	60	0.753±0.054	45.18±6.66
19	≥ 600	12	0.723±0.070	8.68±2.64
low Δm, $N_b = 1$, $N_{SV} = 0$, $M_T(b_{1,2}, \not{E}_T) < 175$ GeV, $300 < p_T(ISR) < 500\,\mathrm{GeV}$, $40 < p_T(b) < 70\,\mathrm{GeV}$				
20	300−400	1613	0.880±0.017	1419.71±45.12
21	400−500	240	0.984±0.044	236.26±18.55
22	500−600	23	0.716±0.066	16.48±3.76
23	≥ 600	7	0.645±0.112	4.52±1.88
low Δm, $N_b = 1$, $N_{SV} = 0$, $M_T(b_{1,2}, \not{E}_T) < 175$ GeV, $p_T(ISR) > 500\,\mathrm{GeV}$, $p_T(b) < 40\,\mathrm{GeV}$				
24	450−550	234	0.683±0.026	159.84±12.07
25	550−650	81	0.771±0.034	62.44±7.46
26	650−750	30	0.741±0.039	22.23±4.22
27	≥ 750	24	0.725±0.037	17.41±3.66
low Δm, $N_b = 1$, $N_{SV} = 0$, $M_T(b_{1,2}, \not{E}_T) < 175$ GeV, $p_T(ISR) > 500\,\mathrm{GeV}$, $40 < p_T(b) < 70\,\mathrm{GeV}$				
28	450−550	145	0.830±0.037	120.37±11.33
29	550−650	53	0.806±0.041	42.72±6.26
30	650−750	18	0.757±0.055	13.63±3.36
31	≥ 750	16	0.881±0.070	14.09±3.70
low Δm, $N_b = 1$, $N_{SV} \geq 1$, $M_T(b_{1,2}, \not{E}_T) < 175$ GeV, $p_T(b) < 40\,\mathrm{GeV}$				
32	300−400	292	0.832±0.039	243.00±18.31
33	400−500	80	0.693±0.056	55.44±7.65
34	≥ 500	33	0.745±0.061	24.57±4.73
low Δm, $N_b \geq 2$, $M_T(b_{1,2}, \not{E}_T) < 175$ GeV, $300 < p_T(ISR) < 500\,\mathrm{GeV}$, $p_T(b_{12}) < 80\,\mathrm{GeV}$				
35	300−400	402	0.727±0.026	292.24±18.05
36	400−500	63	0.783±0.062	49.33±7.33
37	≥ 500	10	0.868±0.167	8.68±3.22
low Δm, $N_b \geq 2$, $M_T(b_{1,2}, \not{E}_T) < 175$ GeV, $300 < p_T(ISR) < 500\,\mathrm{GeV}$, $80 < p_T(b_{12}) < 140\,\mathrm{GeV}$				
38	300−400	863	0.649±0.013	560.16±22.26
39	400−500	159	0.724±0.037	115.13±10.83
40	≥ 500	22	0.532±0.067	11.70±2.89
low Δm, $N_b \geq 2$, $M_T(b_{1,2}, \not{E}_T) < 175$ GeV, $300 < p_T(ISR) < 500\,\mathrm{GeV}$, $p_T(b_{12}) > 140\,\mathrm{GeV}$, $N_j \geq 7$				
41	300−400	550	0.579±0.014	318.38±15.50
42	400−500	96	0.583±0.028	55.96±6.32
43	≥ 500	23	0.927±0.090	21.33±4.91
low Δm, $N_b \geq 2$, $M_T(b_{1,2}, \not{E}_T) < 175$ GeV, $p_T(ISR) > 500\,\mathrm{GeV}$, $p_T(b_{12}) < 80\,\mathrm{GeV}$				
44	450−550	30	0.497±0.048	14.90±3.08
45	550−650	16	0.543±0.073	8.69±2.46
46	≥ 650	2	0.741±0.104	1.48±1.07
low Δm, $N_b \geq 2$, $M_T(b_{1,2}, \not{E}_T) < 175$ GeV, $p_T(ISR) > 500\,\mathrm{GeV}$, $80 < p_T(b_{12}) < 140\,\mathrm{GeV}$				
47	450−550	78	0.567±0.035	44.25±5.71
48	550−650	26	0.758±0.073	19.70±4.30
49	≥ 650	15	0.671±0.076	10.07±2.84
low Δm, $N_b \geq 2$, $M_T(b_{1,2}, \not{E}_T) < 175$ GeV, $p_T(ISR) > 500\,\mathrm{GeV}$, $p_T(b_{12}) > 140\,\mathrm{GeV}$, $N_j \geq 7$				
50	450−550	87	0.495±0.024	43.10±5.07
51	550−650	43	0.639±0.048	27.49±4.67
52	≥ 650	17	0.610±0.057	10.36±2.70

Search region	$\not{E}_T$	singlelep	TF_{LL}	TF_{LL}^{CR-SR}	$TF_{LL}^{SR-extrap}$	N_{pred}^{LL}
high Δm, $N_b = 1$, $M_T(b_{1,2}, \not{E}_T) < 175$ GeV, $N_j \geq 7$, $N_{res} \geq 1$						
53	250−300	4327	0.186±0.003	0.675	0.276	806.44±16.52
54	300−400	2076	0.178±0.003	0.692	0.257	369.44±10.81
55	400−500	366	0.173±0.008	0.730	0.238	63.47±4.39
56	≥ 500	99	0.131±0.010	0.803	0.163	12.96±1.66
high Δm, $N_b \geq 2$, $M_T(b_{1,2}, \not{E}_T) < 175$ GeV, $N_j \geq 7$, $N_{res} \geq 1$						
57	250−300	6511	0.307±0.002	0.686	0.447	1997.45±29.50
58	300−400	3219	0.294±0.003	0.691	0.425	945.02±19.72
59	400−500	507	0.259±0.007	0.688	0.377	131.43±6.84
60	≥ 500	163	0.238±0.012	0.743	0.321	38.82±3.62
high Δm, $N_b = 1$, $M_T(b_{1,2}, \not{E}_T) > 175$ GeV, $N_j \geq 7$, $N_t = 0$, $N_{res} = 0$, $N_W = 0$						
61	250−350	6231	0.299±0.003	0.644	0.465	1864.15±30.25
62	350−450	1269	0.310±0.006	0.663	0.467	393.39±13.67
63	450−550	345	0.310±0.011	0.613	0.505	106.80±6.96
64	≥ 550	169	0.342±0.014	0.609	0.562	57.80±5.04
high Δm, $N_b \geq 2$, $M_T(b_{1,2}, \not{E}_T) > 175$ GeV, $N_j \geq 7$, $N_t = 0$, $N_{res} = 0$, $N_W = 0$						
65	250−350	1450	0.335±0.006	0.687	0.488	486.18±15.55
66	350−450	322	0.322±0.012	0.661	0.487	103.72±6.89
67	450−550	85	0.275±0.017	0.614	0.448	23.37±2.91
68	≥ 550	51	0.233±0.019	0.517	0.450	11.87±1.92
high Δm, $N_b = 1$, $M_T(b_{1,2}, \not{E}_T) > 175$ GeV, $N_t \geq 1$, $N_{res} = 0$, $N_W = 0$, < 1000						
69	250−550	21516	0.030±0.000	0.745	0.040	646.81±10.03
70	550−650	148	0.126±0.010	0.805	0.157	18.66±2.15
71	≥ 650	46	0.121±0.015	0.842	0.143	5.56±1.08
high Δm, $N_b = 1$, $M_T(b_{1,2}, \not{E}_T) > 175$ GeV, $N_t \geq 1$, $N_{res} = 0$, $N_W = 0$, $1000 << 1500$						
72	250−550	960	0.119±0.003	0.728	0.163	113.97±4.98
73	550−650	50	0.087±0.012	0.649	0.135	4.37±0.88
74	≥ 650	61	0.074±0.010	0.662	0.111	4.49±0.86
high Δm, $N_b = 1$, $M_T(b_{1,2}, \not{E}_T) > 175$ GeV, $N_t \geq 1$, $N_{res} = 0$, $N_W = 0$, > 1500						
75	250−550	201	0.170±0.009	0.796	0.213	34.13±3.04
76	550−650	10	0.182±0.037	0.705	0.258	1.82±0.69
77	≥ 650	26	0.070±0.016	0.618	0.114	1.83±0.55
high Δm, $N_b = 1$, $M_T(b_{1,2}, \not{E}_T) > 175$ GeV, $N_t = 0$, $N_{res} = 0$, $N_W \geq 1$, < 1300						
78	250−350	18251	0.072±0.001	0.735	0.099	1322.45±17.10
79	350−450	3312	0.075±0.002	0.780	0.096	247.85±7.29
80	≥ 450	1002	0.058±0.003	0.789	0.074	58.17±3.35
high Δm, $N_b = 1$, $M_T(b_{1,2}, \not{E}_T) > 175$ GeV, $N_t = 0$, $N_{res} = 0$, $N_W \geq 1$, > 1300						
81	250−350	237	0.079±0.006	0.828	0.095	18.63±1.80
82	350−450	100	0.069±0.008	0.748	0.092	6.89±1.07
83	≥ 450	116	0.055±0.007	0.650	0.085	6.41±0.99
high Δm, $N_b = 1$, $M_T(b_{1,2}, \not{E}_T) > 175$ GeV, $N_t = 0$, $N_{res} \geq 1$, $N_W = 0$, < 1000						
84	250−350	17766	0.244±0.002	0.735	0.332	4330.52±42.75
85	350−450	3115	0.208±0.003	0.786	0.265	647.96±15.60
86	450−550	635	0.148±0.006	0.824	0.179	93.71±5.28
87	550−650	148	0.111±0.009	0.805	0.137	16.36±1.88
88	≥ 650	46	0.065±0.010	0.842	0.077	2.99±0.62
high Δm, $N_b = 1$, $M_T(b_{1,2}, \not{E}_T) > 175$ GeV, $N_t = 0$, $N_{res} \geq 1$, $N_W = 0$, $1000 << 1500$						
89	250−350	597	0.114±0.004	0.745	0.153	68.13±3.76
90	350−450	246	0.114±0.007	0.730	0.156	28.04±2.50
91	450−550	117	0.086±0.008	0.629	0.137	10.07±1.34
92	550−650	50	0.130±0.016	0.649	0.200	6.49±1.22
93	≥ 650	61	0.072±0.009	0.662	0.109	4.40±0.81
high Δm, $N_b = 1$, $M_T(b_{1,2}, \not{E}_T) > 175$ GeV, $N_t = 0$, $N_{res} \geq 1$, $N_W = 0$, > 1500						
94	250−350	125	0.056±0.006	0.856	0.066	7.02±1.00
95	350−450	51	0.057±0.009	0.691	0.083	2.91±0.63
96	450−550	25	0.076±0.014	0.731	0.104	1.90±0.53
97	550−650	10	0.055±0.021	0.705	0.079	0.55±0.27
98	≥ 650	26	0.073±0.019	0.618	0.118	1.89±0.63
high Δm, $N_b = 1$, $M_T(b_{1,2}, \not{E}_T) > 175$ GeV, $N_t \geq 1$, $N_{res} = 0$, $N_W \geq 1$						
99	250−550	22677	0.001±0.000	0.745	0.001	15.57±1.31
100	≥ 550	341	0.001±0.000	0.741	0.002	0.43±0.17

Search region	$\not{E}_T$	singlelep	TF_{LL}	TF_{LL}^{CR-SR}	$TF_{LL}^{SR-extrap}$	N_{pred}^{LL}
high Δm, $N_b = 1$, $M_T(b_{1,2}, \not{E}_T) > 175$ GeV, $N_t \geq 1$, $N_{res} \geq 1$, $N_W = 0$						
101	250−550	22677	0.001±0.000	0.745	0.001	11.50±1.14
102	≥ 550	341	0.002±0.001	0.741	0.003	0.78±0.25
high Δm, $N_b = 1$, $M_T(b_{1,2}, \not{E}_T) > 175$ GeV, $N_t = 0$, $N_{res} \geq 1$, $N_W \geq 1$						
103	250−550	22677	0.003±0.000	0.745	0.004	73.10±2.95
104	≥ 550	341	0.005±0.001	0.741	0.007	1.69±0.46
high Δm, $N_b = 2$, $M_T(b_{1,2}, \not{E}_T) > 175$ GeV, $N_t = 1$, $N_{res} = 0$, $N_W = 0$, < 1000						
105	250−550	3292	0.034±0.001	0.754	0.045	111.61±4.08
106	550−650	31	0.104±0.019	0.706	0.147	3.22±0.82
107	≥ 650	11	0.135±0.035	0.855	0.158	1.49±0.59
high Δm, $N_b = 2$, $M_T(b_{1,2}, \not{E}_T) > 175$ GeV, $N_t = 1$, $N_{res} = 0$, $N_W = 0$, 1000 << 1500						
108	250−550	201	0.160±0.008	0.789	0.203	32.16±2.79
109	550−650	10	0.044±0.015	0.510	0.087	0.44±0.20
110	≥ 650	13	0.161±0.038	0.751	0.214	2.09±0.76
high Δm, $N_b = 2$, $M_T(b_{1,2}, \not{E}_T) > 175$ GeV, $N_t = 1$, $N_{res} = 0$, $N_W = 0$, > 1500						
111	250−550	51	0.204±0.020	0.880	0.232	10.42±1.78
112	550−650	4	0.030±0.021	0.385	0.078	0.12±0.10
113	≥ 650	5	0.119±0.035	0.458	0.261	0.60±0.32
high Δm, $N_b = 2$, $M_T(b_{1,2}, \not{E}_T) > 175$ GeV, $N_t = 0$, $N_{res} = 0$, $N_W = 1$, < 1300						
114	250−350	2778	0.068±0.002	0.760	0.089	188.20±6.22
115	350−450	528	0.070±0.004	0.763	0.091	36.82±2.66
116	≥ 450	193	0.050±0.005	0.684	0.073	9.67±1.20
high Δm, $N_b = 2$, $M_T(b_{1,2}, \not{E}_T) > 175$ GeV, $N_t = 0$, $N_{res} = 0$, $N_W = 1$, > 1300						
117	250−350	67	0.100±0.012	0.865	0.115	6.68±1.16
118	350−450	24	0.049±0.013	0.821	0.060	1.18±0.40
119	≥ 450	28	0.063±0.014	0.556	0.113	1.76±0.52
high Δm, $N_b = 2$, $M_T(b_{1,2}, \not{E}_T) > 175$ GeV, $N_t = 0$, $N_{res} = 1$, $N_W = 0$, < 1000						
120	250−350	2675	0.202±0.003	0.757	0.268	541.50±13.94
121	350−450	495	0.186±0.007	0.763	0.243	92.02±5.47
122	450−550	122	0.143±0.012	0.660	0.217	17.46±2.14
123	550−650	31	0.106±0.018	0.706	0.150	3.29±0.81
124	≥ 650	11	0.173±0.042	0.855	0.203	1.91±0.74
high Δm, $N_b = 2$, $M_T(b_{1,2}, \not{E}_T) > 175$ GeV, $N_t = 0$, $N_{res} = 1$, $N_W = 0$, 1000 << 1500						
125	250−350	139	0.157±0.010	0.817	0.192	21.84±2.33
126	350−450	42	0.104±0.012	0.741	0.140	4.36±0.84
127	450−550	20	0.098±0.017	0.740	0.132	1.96±0.55
128	550−650	10	0.092±0.023	0.510	0.181	0.92±0.37
129	≥ 650	13	0.146±0.035	0.751	0.194	1.89±0.69
high Δm, $N_b = 2$, $M_T(b_{1,2}, \not{E}_T) > 175$ GeV, $N_t = 0$, $N_{res} = 1$, $N_W = 0$, > 1500						
130	250−350	31	0.107±0.017	0.897	0.119	3.31±0.80
131	350−450	15	0.083±0.026	0.963	0.086	1.25±0.51
132	450−550	5	0.046±0.018	0.662	0.069	0.23±0.14
133	550−650	4	0.016±0.009	0.385	0.042	0.07±0.05
134	≥ 650	5	0.004±0.001	0.458	0.009	0.02±0.01
high Δm, $N_b = 2$, $M_T(b_{1,2}, \not{E}_T) > 175$ GeV, $N_t = 1$, $N_{res} = 0$, $N_W = 1$						
135	250−550	3544	0.000±0.000	0.758	0.000	1.15±0.27
136	≥ 550	74	0.001±0.000	0.650	0.001	0.06±0.03
high Δm, $N_b = 2$, $M_T(b_{1,2}, \not{E}_T) > 175$ GeV, $N_t = 0$, $N_{res} = 1$, $N_W = 1$						
137	250−550	3544	0.004±0.000	0.758	0.005	13.73±1.21
138	≥ 550	74	0.002±0.001	0.650	0.004	0.18±0.11
high Δm, $N_b = 2$, $M_T(b_{1,2}, \not{E}_T) > 175$ GeV, $N_t = 1$, $N_{res} = 1$, $N_W = 0$, < 1300						
139	250−350	2778	0.002±0.000	0.760	0.002	4.61±0.70
140	350−450	528	0.002±0.001	0.763	0.002	0.91±0.30
141	≥ 450	193	0.008±0.002	0.684	0.012	1.57±0.38
high Δm, $N_b = 2$, $M_T(b_{1,2}, \not{E}_T) > 175$ GeV, $N_t = 1$, $N_{res} = 1$, $N_W = 0$, > 1300						
142	250−350	67	0.008±0.003	0.865	0.010	0.56±0.21
143	350−450	24	0.008±0.007	0.821	0.010	0.20±0.17
144	≥ 450	28	0.017±0.007	0.556	0.030	0.47±0.20
high Δm, $N_b = 2$, $M_T(b_{1,2}, \not{E}_T) > 175$ GeV, $N_t = 2$, $N_{res} = 0$, $N_W = 0$, < 1300						
145	250−450	3306	0.000±0.000	0.760	0.000	0.34±0.17
146	450−600	160	0.000±0.000	0.683	0.000	0.00±0.01
147	≥ 600	33	0.000±0.000	0.687	0.000	0.00±0.00
high Δm, $N_b = 2$, $M_T(b_{1,2}, \not{E}_T) > 175$ GeV, $N_t = 2$, $N_{res} = 0$, $N_W = 0$, > 1300						
148	250−450	91	0.001±0.001	0.851	0.002	0.13±0.08
149	450−600	17	0.012±0.008	0.644	0.018	0.20±0.14
150	≥ 600	11	0.000±0.000	0.446	0.001	0.00±0.00
high Δm, $N_b = 2$, $M_T(b_{1,2}, \not{E}_T) > 175$ GeV, $N_t = 0$, $N_{res} = 2$, $N_W = 0$, < 1300						
151	250−450	3306	0.006±0.000	0.760	0.008	19.99±1.62
152	450−600	160	0.007±0.002	0.683	0.010	1.06±0.32
153	≥ 600	33	0.005±0.003	0.687	0.007	0.17±0.11

Search region	$\not{E}_T$	singlelep	TF_{LL}	TF_{LL}^{CR-SR}	$TF_{LL}^{SR-extrap}$	N_{pred}^{LL}
high Δm, $N_b = 2$, $M_T(b_{1,2}, \not{E}_T) > 175$ GeV, $N_t = 0$, $N_{res} = 2$, $N_W = 0$, > 1300						
154	250−450	91	0.005±0.002	0.851	0.006	0.44±0.18
155	450−600	17	0.001±0.000	0.644	0.001	0.01±0.01
156	≥ 600	11	0.009±0.007	0.446	0.021	0.10±0.08
high Δm, $N_b = 2$, $M_T(b_{1,2}, \not{E}_T) > 175$ GeV, $N_t = 0$, $N_{res} = 0$, $N_W = 2$						
157	≥ 250	3618	0.001±0.000	0.756	0.001	2.48±0.52
high Δm, $N_b = 2$, $M_T(b_{1,2}, \not{E}_T) > 175$ GeV, $N_t + N_{res} + N_W >= 3$, < 1300						
158	250−400	3128	0.000±0.000	0.760	0.000	0.37±0.19
159	≥ 400	371	0.000±0.000	0.718	0.000	0.00±0.00
high Δm, $N_b = 2$, $M_T(b_{1,2}, \not{E}_T) > 175$ GeV, $N_t + N_{res} + N_W >= 3$, > 1300						
160	250−400	83	0.000±0.000	0.845	0.000	0.00±0.00
161	≥ 400	36	0.001±0.001	0.638	0.002	0.04±0.03
high Δm, $N_b \geq 3$, $M_T(b_{1,2}, \not{E}_T) > 175$ GeV, $N_t = 1$, $N_{res} = 0$, $N_W = 0$, < 1000						
162	250−350	515	0.032±0.003	0.850	0.037	16.41±1.64
163	350−550	114	0.087±0.009	0.829	0.105	9.90±1.38
164	≥ 550	8	0.092±0.029	0.657	0.140	0.74±0.35
high Δm, $N_b \geq 3$, $M_T(b_{1,2}, \not{E}_T) > 175$ GeV, $N_t = 1$, $N_{res} = 0$, $N_W = 0$, $1000 << 1500$						
165	250−350	50	0.121±0.017	0.720	0.169	6.07±1.20
166	350−550	22	0.124±0.021	0.673	0.185	2.74±0.75
167	≥ 550	2	0.046±0.026	0.727	0.063	0.09±0.08
high Δm, $N_b \geq 3$, $M_T(b_{1,2}, \not{E}_T) > 175$ GeV, $N_t = 1$, $N_{res} = 0$, $N_W = 0$, > 1500						
168	250−350	12	0.290±0.061	0.912	0.318	3.48±1.24
169	350−550	3	0.262±0.078	0.769	0.341	0.79±0.51
170	≥ 550	3	0.032±0.028	0.416	0.077	0.10±0.10
high Δm, $N_b \geq 3$, $M_T(b_{1,2}, \not{E}_T) > 175$ GeV, $N_t = 0$, $N_{res} = 0$, $N_W = 1$						
171	250−350	577	0.072±0.004	0.839	0.086	41.73±2.89
172	350−550	139	0.059±0.006	0.797	0.074	8.23±1.12
173	≥ 550	13	0.049±0.016	0.642	0.077	0.64±0.27
high Δm, $N_b \geq 3$, $M_T(b_{1,2}, \not{E}_T) > 175$ GeV, $N_t = 0$, $N_{res} = 1$, $N_W = 0$, < 1000						
174	250−350	515	0.207±0.008	0.850	0.244	106.80±6.13
175	350−550	114	0.191±0.015	0.829	0.230	21.76±2.66
176	≥ 550	8	0.083±0.031	0.657	0.126	0.66±0.34
high Δm, $N_b \geq 3$, $M_T(b_{1,2}, \not{E}_T) > 175$ GeV, $N_t = 0$, $N_{res} = 1$, $N_W = 0$, $1000 << 1500$						
177	250−350	50	0.143±0.017	0.720	0.199	7.16±1.33
178	350−550	22	0.147±0.025	0.673	0.218	3.23±0.88
179	≥ 550	2	0.157±0.060	0.727	0.216	0.31±0.25
high Δm, $N_b \geq 3$, $M_T(b_{1,2}, \not{E}_T) > 175$ GeV, $N_t = 0$, $N_{res} = 1$, $N_W = 0$, > 1500						
180	250−350	12	0.127±0.036	0.912	0.139	1.52±0.62
181	350−550	3	0.045±0.023	0.769	0.058	0.13±0.10
182	≥ 550	3	0.160±0.078	0.416	0.384	0.48±0.36
high Δm, $N_b \geq 3$, $M_T(b_{1,2}, \not{E}_T) > 175$ GeV, $N_t = 1$, $N_{res} = 0$, $N_W = 1$						
183	250−500	708	0.001±0.000	0.838	0.002	0.89±0.25
184	≥ 500	21	0.001±0.001	0.569	0.002	0.02±0.02
high Δm, $N_b \geq 3$, $M_T(b_{1,2}, \not{E}_T) > 175$ GeV, $N_t = 0$, $N_{res} = 1$, $N_W = 1$						
185	250−500	708	0.005±0.001	0.838	0.006	3.29±0.61
186	≥ 500	21	0.000±0.000	0.569	0.000	0.00±0.00
high Δm, $N_b \geq 3$, $M_T(b_{1,2}, \not{E}_T) > 175$ GeV, $N_t = 1$, $N_{res} = 1$, $N_W = 0$, < 1300						
187	250−350	557	0.002±0.001	0.840	0.002	1.14±0.34
188	350−500	125	0.010±0.003	0.838	0.012	1.30±0.38
189	≥ 500	18	0.013±0.007	0.578	0.023	0.24±0.14
high Δm, $N_b \geq 3$, $M_T(b_{1,2}, \not{E}_T) > 175$ GeV, $N_t = 1$, $N_{res} = 1$, $N_W = 0$, > 1300						
190	250−350	20	0.018±0.008	0.826	0.021	0.35±0.18
191	350−500	6	0.001±0.000	0.758	0.001	0.00±0.00
192	≥ 500	3	0.023±0.017	0.533	0.044	0.07±0.07
high Δm, $N_b \geq 3$, $M_T(b_{1,2}, \not{E}_T) > 175$ GeV, $N_t = 2$, $N_{res} = 0$, $N_W = 0$, < 1300						
193	250−500	682	0.000±0.000	0.839	0.000	0.02±0.01
194	≥ 500	18	0.000±0.000	0.578	0.000	0.00±0.00
high Δm, $N_b \geq 3$, $M_T(b_{1,2}, \not{E}_T) > 175$ GeV, $N_t = 2$, $N_{res} = 0$, $N_W = 0$, > 1300						
195	250−500	26	0.001±0.000	0.801	0.001	0.02±0.01
196	≥ 500	3	0.001±0.001	0.533	0.002	0.00±0.00
high Δm, $N_b \geq 3$, $M_T(b_{1,2}, \not{E}_T) > 175$ GeV, $N_t = 0$, $N_{res} = 2$, $N_W = 0$, < 1300						
197	250−500	682	0.007±0.001	0.839	0.008	4.56±0.68
198	≥ 500	18	0.000±0.000	0.578	0.000	0.00±0.01
high Δm, $N_b \geq 3$, $M_T(b_{1,2}, \not{E}_T) > 175$ GeV, $N_t = 0$, $N_{res} = 2$, $N_W = 0$, > 1300						
199	250−500	26	0.009±0.005	0.801	0.011	0.24±0.13
200	≥ 500	3	0.001±0.001	0.533	0.002	0.00±0.00
high Δm, $N_b \geq 3$, $M_T(b_{1,2}, \not{E}_T) > 175$ GeV, $N_t = 0$, $N_{res} = 0$, $N_W = 2$						
201	≥ 250	729	0.001±0.001	0.825	0.001	0.82±0.37
high Δm, $N_b \geq 3$, $M_T(b_{1,2}, \not{E}_T) > 175$ GeV, $N_t + N_{res} + N_W >= 3$						
202	250−400	652	0.000±0.000	0.844	0.000	0.18±0.12
203	≥ 400	77	0.001±0.001	0.703	0.001	0.07±0.05

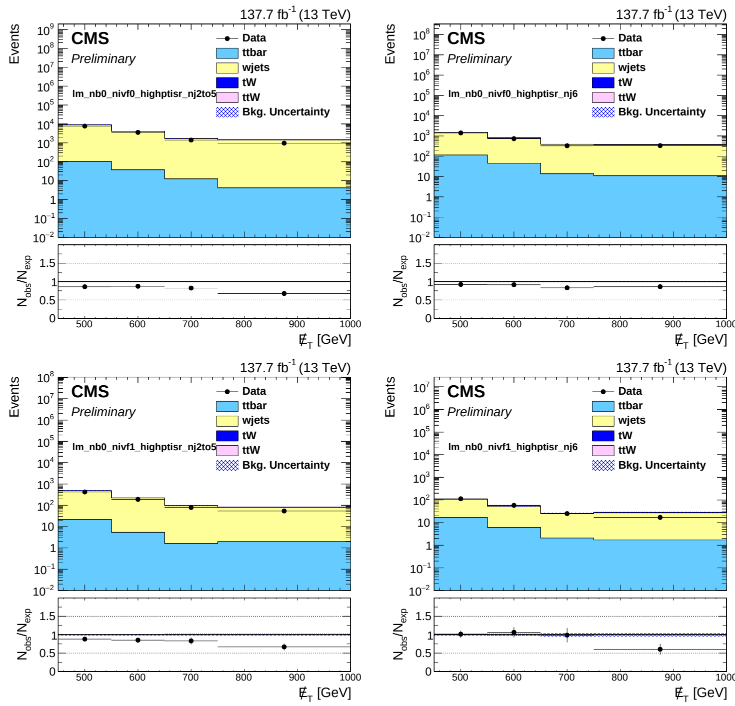

Figure 5.1 : Comparison of the $\not{E}_T$ distribution in the single-lepton sample after applying the low Δm baseline selection in the $N_b = 0$ region. Data and simulation are represented by the black points and stacked histograms, respectively. The error bars on the ratio of observed data to simulation correspo nd to the data statistical uncertainty and the shaded blue band represents the statistical uncertainty on the simulation. These regions are included with the search regions in the simultaneous fit for the signal extraction in order to estimate the LL contribution.

5.2.2 Z Boson Decay to Neutrinos

An important source of background for the zero-lepton search is from events in which a Z boson, produced in association with jets, decays to neutrinos that result in a significant amount of missing energy in the event. Two methods are traditionally used to estimate the $Z \to \nu\nu$ background. The first method makes use of a sample dominated by $Z \to ll$+jets events. This approach comes with the advantage of very similar kinematics (after correcting for the difference in acceptance between charged lepton pairs and pairs of neutrinos), but is statistically limited, especially in the tight search regions used in SUSY searches. The second method utilizes a γ+jets sample. The γ+jets process has a factor of 5 or more larger cross section than the $Z \rightarrow ll$+jets process, and has similar leading order Feynman diagrams to Z+jets events. However, there are two main differences between the two processes that must be taken into account, namely, different quark-boson couplings and the fact that the Z boson is very massive. Both of these effects become less important with higher boson p_T, which is the kinematic region we are probing with this search. The $\not{E}_T$ of the γ+jets process is calculated after removing the photon from the event to mimic the $Z \rightarrow \nu\nu$ process.

Based on the above, we use a hybrid method to estimate the $Z \rightarrow \nu\nu$ background that makes use of both the γ+jets and the $Z \rightarrow ll$+jets processes. The photon and the dilepton system are removed from the events before calculating $\not{E}_T$ and other kinematic variables related to $\not{E}_T$, and the modified $\not{E}_T$ is denoted by $\not{E}_T^{\gamma}$ and $\not{E}_T^{ll}$ for γ+jets and the $Z \rightarrow ll$+jets processes, respectively. We utilize the $Z \rightarrow ll$+jets sample to measure the normalization of the $Z \rightarrow \nu\nu$ process in different ranges of N_b and N_{SV}, andwe take advantage of the much higher statistics of the γ+jets sample to extract shape corrections. As discussed in Sec. , the good agreement we observe between data and simulation in the Lost Lepton background leads us to integrate the control regions used in the estimation of the $Z \rightarrow \nu\nu$ background in the number of t and W tags to increase the statistical power of the prediction. We then extrapolate into tagged regions using simulation, corrected with the appropriate t and W tagging data-to-simulation scale factors.

The prediction of the $Z \to \nu\nu$ background is given by:

$$N_{pred}^{Z\to\nu\nu} = N_{MC}^{Z\to\nu\nu} \cdot R_Z \cdot S_\gamma \tag{5.3}$$

Znunu: production of a Z boson that decays into two nuetrinos which are then missed by the detector. Can have jets from other quarks/gluons in the interaction

5.2.3 Quantum Chromodynamic Events

Simulation predicts negligible levels of QCD contamination in the various search regions. However, the QCD multijet simulation has limited statistics and there are uncertainties related to the description of physics in the simulation, particularly for the rare scenarios that would lead to a multijet event passing all of the final search region selection criteria. For these reasons, it is necessary to perform a data-driven QCD background estimation. We follow an approach similar to those described for other SM backgrounds, first using a QCD-enhanced region to validate the simulation, then extrapolating the event count in the control region to a prediction in the search region.

$\not{E}_T$ is generated in QCD events through either jet p_T mis-measurement or semileptonic heavy flavor decay and for the purposes of this section both sources of $\not{E}_T$ will be generally referred to as "mis-measurement". This leads to the characteristic of $\not{E}_T$ being aligned to one of the leading jets, which motivates including a veto on such events in the baseline selection. On the other hand, inverting and tightening the $\Delta\phi_{1234} > 0.5$ selection from the high Δm region, or the $|\Delta\phi(j_1, \not{E}_T)| > 0.5$, $|\Delta\phi(j_{2,3}, \not{E}_T)| > 0.15$ selection from the low Δm region, to $\Delta\phi_{123} < 0.1$ for both the high and low Δm regions result in regions with fairly pure samples of QCD events. The QCD search regions yields are estimated with data yields in a series of control regions with this modified baseline selection after subtracting the contamination of non-QCD processes. The control region yields are related to search region yields with the following simulation transfer factors:

$$TF_{QCD} = \frac{N_{MC}^{QCD}(SR)}{N_{MC}^{QCD}(\Delta\phi_{123} < 0.1)} \tag{5.4}$$

where $N_{MC}^{QCD}(SR)$ are the expected QCD yields from simulation for the signal regions, ($\Delta\phi_{1234} > 0.5$ for high Δm and $|\Delta\phi(j_1, \not{E}_T)| > 0.5$, $|\Delta\phi(j_{2,3}, \not{E}_T)| > 0.15$ for low Δm) and $N_{MC}^{QCD}(\Delta\phi_{123} < 0.1)$ is the expected QCD yield from simulation for the control region. The QCD estimate, N_{pred}^{QCD}, is defined as:

$$N_{pred}^{QCD} = TF_{QCD} \cdot (N_{data} - N_{MC}^{non-QCD}), \tag{5.5}$$

where N_{data} is the number of events in the $\Delta\phi_{123} < 0.1$ control sample described above, and $N_{MC}^{non-QCD}$ is the number of non-QCD events in this sample as estimated by the background predictions.

For the estimation of the QCd contribution in the high Δm search regions, the QCD control regions match the selection in the corresponding search regions except from the selection on N_t, N_W, and N_{res}. Binning the control regions in these dimensions has the advantage of measureming the efficiency of each variable directly in data. The t and W tags improves significantly the statistical power of the estimate. The lepton vetoes are not applied when calculating TF_{QCD}, only on N_{data} and $N_{MC}^{non-QCD}$. The fake rates are then estimated directly from data.

A similar approach is utilized for the estimation of the QCD contribution in the low Δm search regions. The QCD control regions are binned in the same variables and ranges as of the search regions, but the QCD purity is low for the low Δm

control regions with one or more b-tags (the high Δm control regions are integrated with respect to top and W-tags and therefore have sufficient statistics in spite of the number of b-tags). Except for a normalization factor, the MC is generally consistent with data as function of $\not{E}_T$ for each of the control regions. Therefore, these low Δm control region $\not{E}_T$ bins are combined in order to increase the precision of the prediction in these search region bins. A systematic uncertainty on this integration is obtained by comparing the MC $\not{E}_T$ shape to the data shape for the two $N_b = 0$ control regions in which no integration is applied. For each control region, the data to MC ratio for each $\not{E}_T$ bin is compared to the fully integrated ratio. The maximum difference, 51% is the systematic uncertainty.

QCD events fail the $\Delta\phi_{1234} > 0.5$ or $|\Delta\phi(j_1, \not{E}_T)| > 0.5$, $|\Delta\phi(j_{2,3}, \not{E}_T)| > 0.15$ selection cuts, for the high and low Δm regions respectively, and enter the search region due to a leading jet undergoing such severe mis-measurement that it is reconstructed as one of the sub-leading jets. Mis-measurement is parameterized by the jet response, defined as:

$$r_{jet} = \frac{p_{T\,reco}}{p_{T\,gen}}. \tag{5.6}$$

A much larger proportion of events in the search region that the control region are in the tail of the r_{jet} distribution, which means that this method relies on the correct modeling of r_{jet} in simulation. Therefore, a r_{jet} correction and uncertainty is extracted from data using the method described in Ref. []. The correciton is derived with the pseudo jet response ($r_{pseudo,jet}$) distribution, applying the QCD control region selection except for the number of jets and b-tagging requirements. We divide this region into two, in the case of the jet aligned to $\not{E}_T$ passing the medium b-tag requirement and in the case of it not passing the light b-tag requirement. The corrections range between 0.81 ± 0.12 and 0.83 ± 0.08 in the case of jets originating from b-quarks and between 1.04 ± 0.04 and 1.82 ± 0.15 for all other jets as can be seen in Table .

The statistical uncertainty on TF_{QCD} is reduced by increasing the effective luminosity of the QCD multijet sample with a method referring to as "local smearing." The method relies on the parametrization of r_{jet}, which is only dependent on jet properties.

5.2.3.1 QCD Local Smearing

Write smearing method here.

5.2.3.2 QCD Corrections

Figures ? and ? show the $\not{E}_T$ distribution in data and simulation in the QCD control regions for the high Δm and lowd Δm selections, respectively. The stacked plot labeled "Non-QCD bkg" is the distribution of the non-QCD events as predicted with the estimation methods detailed in this note. The other stacked plot, labeled "Smeared QCD MC" is the smeared QCD simulation yield after applying the r_{jet} corrections. The other two lines show a combination of the predicted non-QCD SM yields and one of two scenarios. "Without r_{jet} corr" is the smeared QCD simulation without the r_{jet} correction and "With orig. QCD MC" is the standard QCD simulation without this correction. There are three important trends in this figure. The first is the purity of the control regions, which gives confidence in using them to predict QCD yields. The second is that the "Without r_{jet} corr" estimation is nearly equivalent to "With orig. QCD MC" in the regions where there are enough statistics to have a meaningful comparison. This improves our confidence in the use of the smeared QCD simulation. Finally, the r_{jet} correction improves the agreement between data simulation, which is a useful validation of this correction. Due to the nature of the background estimation method applied in the high Δm search, control regions are utilized for the prediciton of multiple search regions.

Tables ? and ? summarize the yields in data, the derived transfer factors, and the resulting QCD predictions for the high Δm and low Δm search regions respectively. The transfer factors in the high Δm region actually account for two levels of extrapolation, i.e., the extrapolation from the control regions to the search regions without the requirement of top and W tags, and the extrapolation in top and W tags in the search regions after correcting the top- and W-tagging efficiencies:

$$TF_{QCD} = TF_{QCD}^{CR-SR} \times TF_{QCD}^{SR-extrap} = \frac{N_{MC}(SR)(N_j, N_b, \not{E}_T)}{N_{MC}(\Delta\phi_{123} < 0.1)(N_j, N_b, \not{E}_T)} \times \frac{N_{MC}(SR)(N_j, N_b, \not{E}_T, N_t, N_{res},}{N_{MC}(SR)(N_j, N_b, \not{E}_T)} \tag{5.7}$$

5.2.4 Rare Interactions

The contributions of diboson (WW, WZ, and ZZ) processes are relatively small compared to the other backgrounds, and mainly affect the search regions targeting low Δm signal models. The prediciton of the diboson background is obtained directly from simulation, and an uncertainty of 50% is assigned on the cross section.

The contribution of the ttZ background is also generally very small due to the rarity of this process. However, in search regions that require the presence of more than one top- or W-tagged candidates, this process can constitute a significant fraction of the total SM background due to the strong suppression of the other SM processes. In order to validate the prediction of this background, we define a three-lepton control sample, selected using single-lepton triggers, which requires the presence of exactly three electrons or muons satisfying p_T> 40 GeV for the leading lepton, p_T> 20 GeV for the second and third leptons, and no additional lepton with p_T> 10 GeV. We further require at least five jets, at least two of which are b-tagged. A Z boson mass window of 81-101 GeV is placed on the invariant mass of the same-flavor dilepton p_T of this lepton pair is further required to be at least 100 GeV, in order to probe a kinematic region close to the one relevant for the analysis. Figure ? shows the reconstructed Z boson p_T distribution observed in this sample. We use the region outside the Z boson mass window (the $\not{E}_T$ distribution in this region is also shown in Fig. ?) to simultaneously constrain the $t\bar{t}$background consisting of dilepton $t\bar{t}$events with an additional lepton originating from semi-leptonic b-hadron decay or from a misidentified jet, and obtain a scale factor of 1.10 ± 0.26 for the ttZ-like processes in this sample, where the uncertainty is dominated by the statistical uncertainty in the data sample. We therefore apply an uncertainty of 24% to the normalization of the ttZ background in the analysis. In order to check the extrapolation from the lower Z-p_T region of this control sample to the search sample, we evaluate the ttZ scale factor in bins of reconstructed Z boson p_T as far as statistics permit. The p_T-binned scale factors are found to be consistent with the inclusive scale factor evaluated for $p_T(Z) > 100$ GeV (Fig. sldkjf). Additional experimental and theoretical uncertainties related to PDF and factorization/renormalization scale variations are also assigned. Figure ? shows the number of top- and W-tagged events observed in the ttZ control sample.

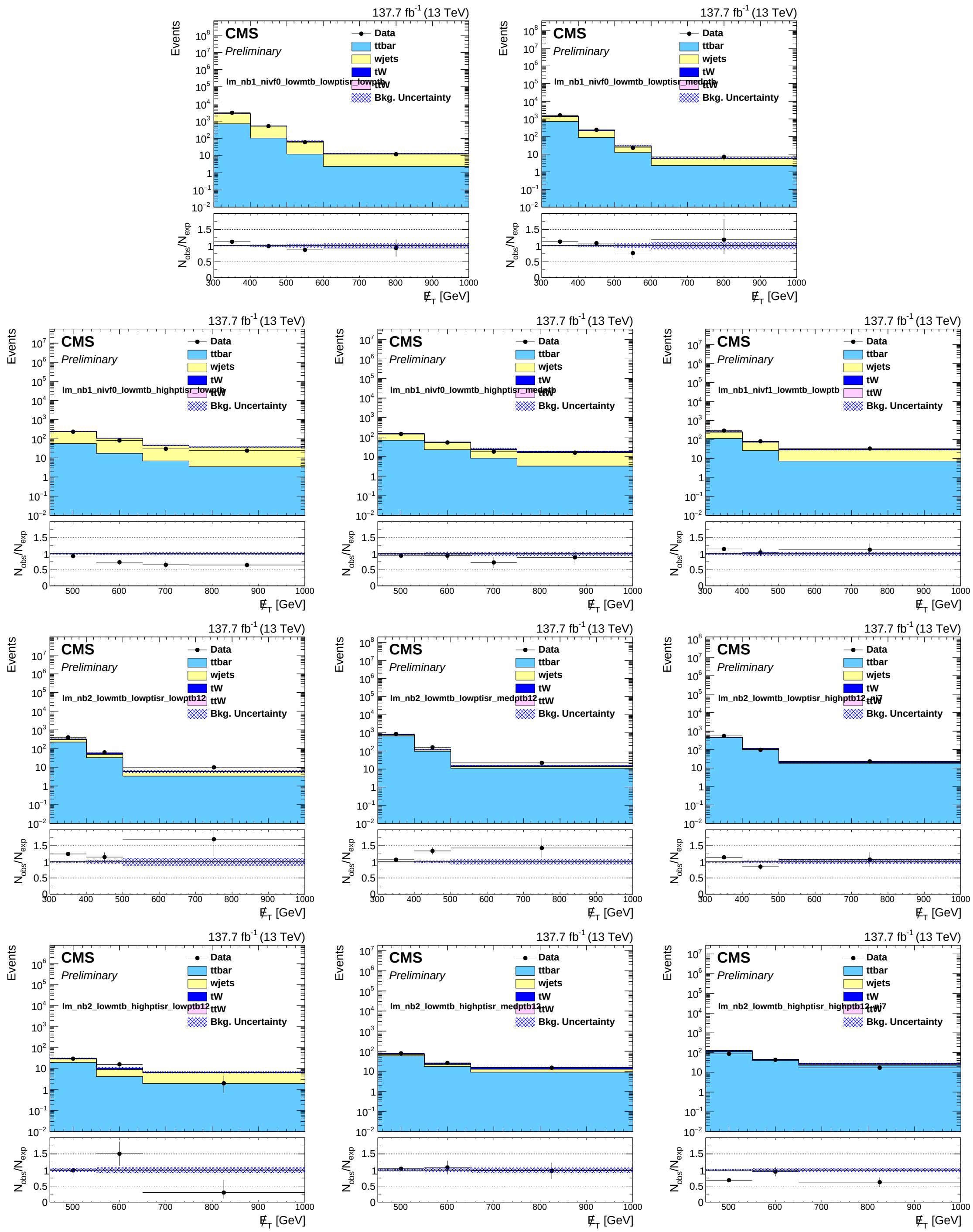

Figure 5.2 : Comparison of the $\not\!\!E_T$ distribution in the single-lepton sample after applying the low Δm baseline selection. Two top rows: Events with $N_b = 1$; Two bottom rows: Events with $N_b \geq 2$; Data and simulation are represented by the black points and stacked histograms, respectively. The error b ars on the ratio of observed data to simulation correspond to the data statistical uncertainty and the shaded blue band represents the statistical uncertainty on the simulation. These regions are included with the search regions in the simultaneous fit for the signal extraction in order to estimate the LL contribution.

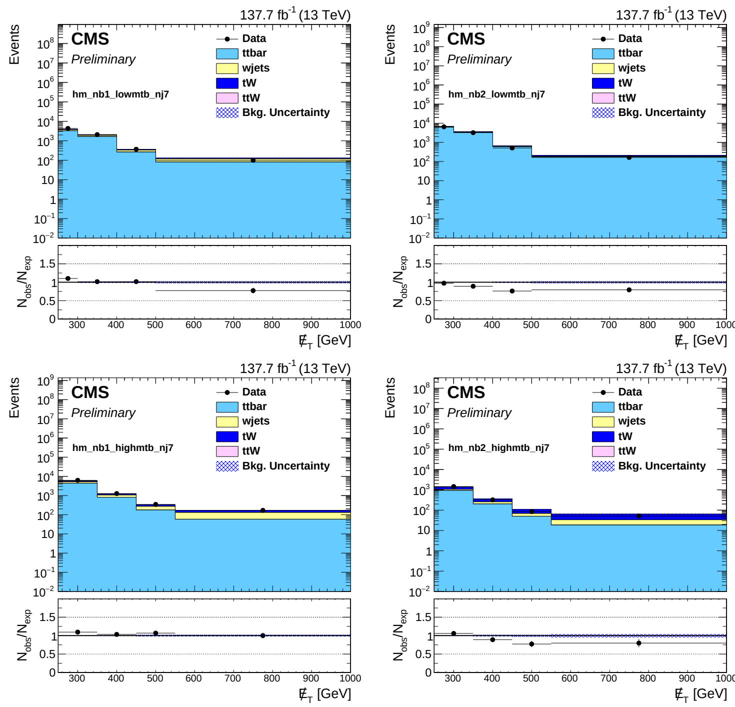

Figure 5.3 : Comparison of the $\not{E}_T$ distribution in the single-lepton sample after applying the high Δm baseline selection in the $M_T(b_{1,2}, \not{E}_T) < 175\ GeV$ and $N_t = 0, N_{res} = 0$, and $N_W = 0$ region. Data and simulation are represented by the black points and stacked histograms, respectively. The error bars on the ratio of observed data to simulation correspond to the data statistical uncertainty and the shaded blue band represents the statistical uncertainty on the simulation. These regions are included with the search regions in the simultaneous fit for the signal extraction in order to estimate the LL contribution.

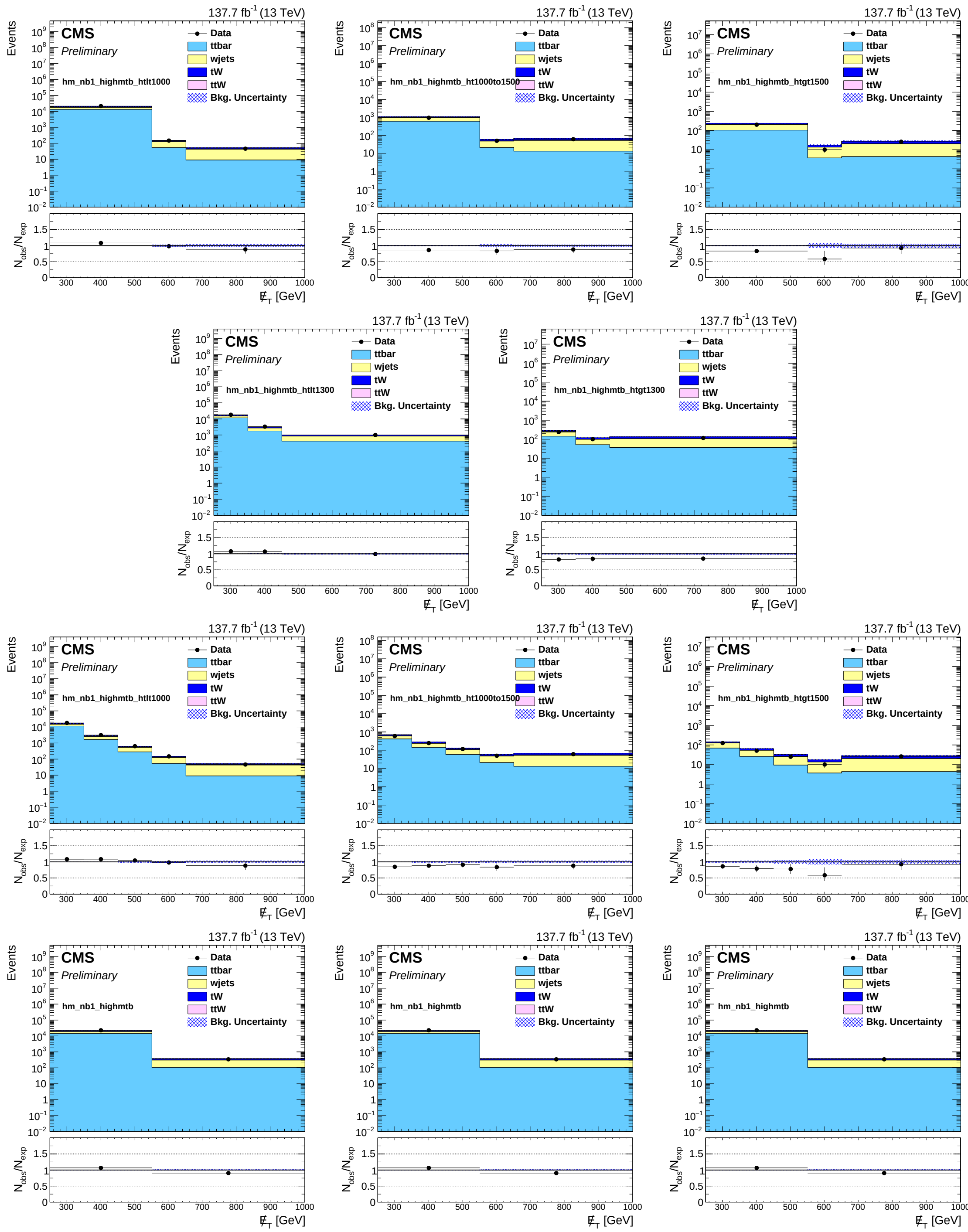

Figure 5.4 : Comparison of the $\not{E}_T$ distribution in the single-lepton sample after applying the high Δm baseline selection in the $N_b = 1$ region where there are ≥ 1 heavy object tags. Data and simulation are represented by the black points and stacked histograms, respectively. The error bars on the ratio of observed data to simulation correspo nd to the data statistical uncertainty and the shaded blue band represents the statistical uncertainty on the simulation. These regions are included with the search regions in the simultaneous fit for the signal extraction in order to estimate the LL contribution.

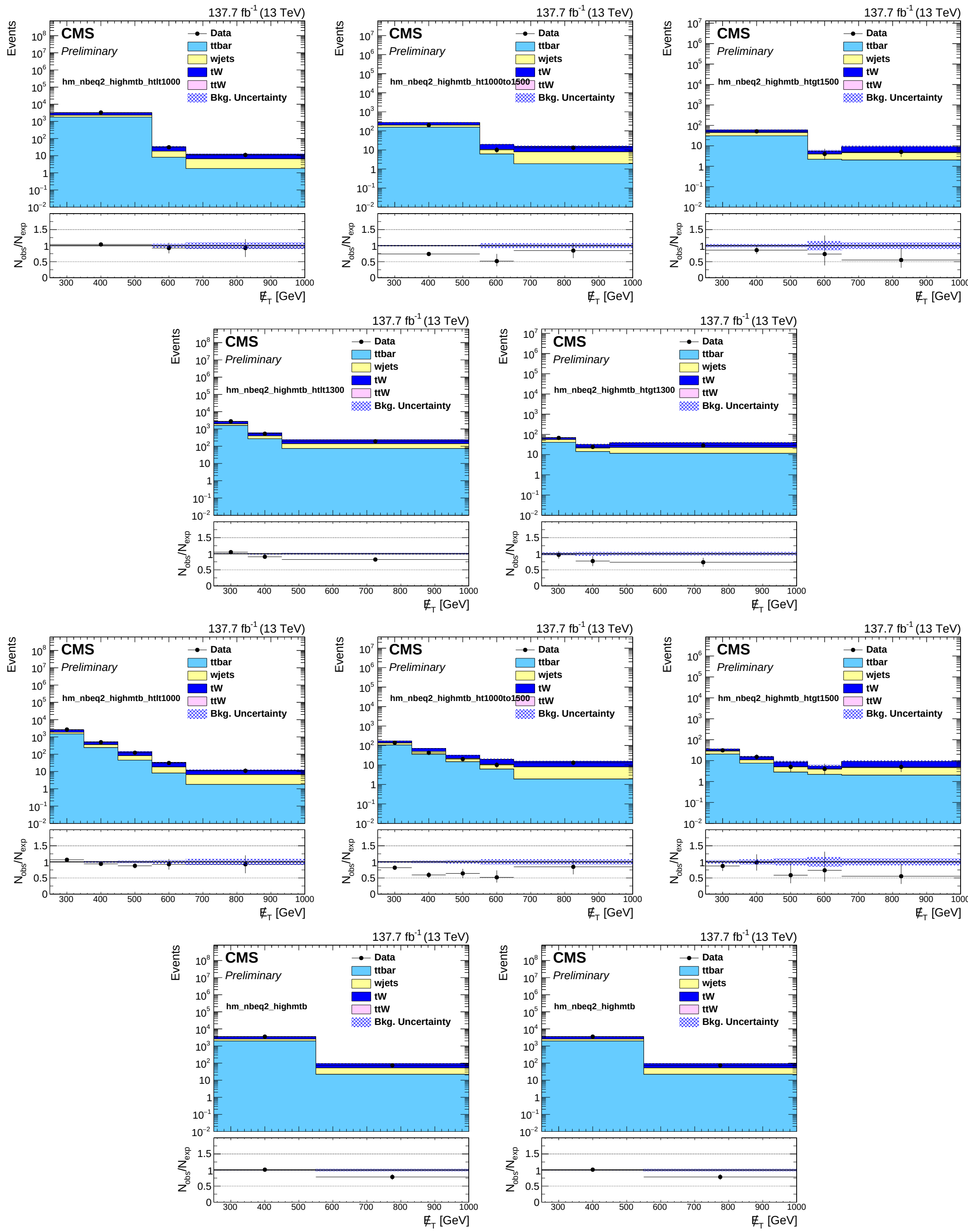

Figure 5.5 : Comparison of the $\not\!\!E_T$ distribution in the single-lepton sample after applying the high Δm baseline selection in the $N_b = 2$ and $N_t = 1, N_{res} = 1$, or $N_W = 1$ regions. Data and simulation are represented by the black points and stacked histograms, respectively. The error bars on the ratio of observed data to simulation correspo nd to the data statistical uncertainty and the shaded blue band represents the statistical uncertainty on the simulation. These regions are included with the search regions in the simultaneous fit for the signal extraction in order to estimate the LL contribution.

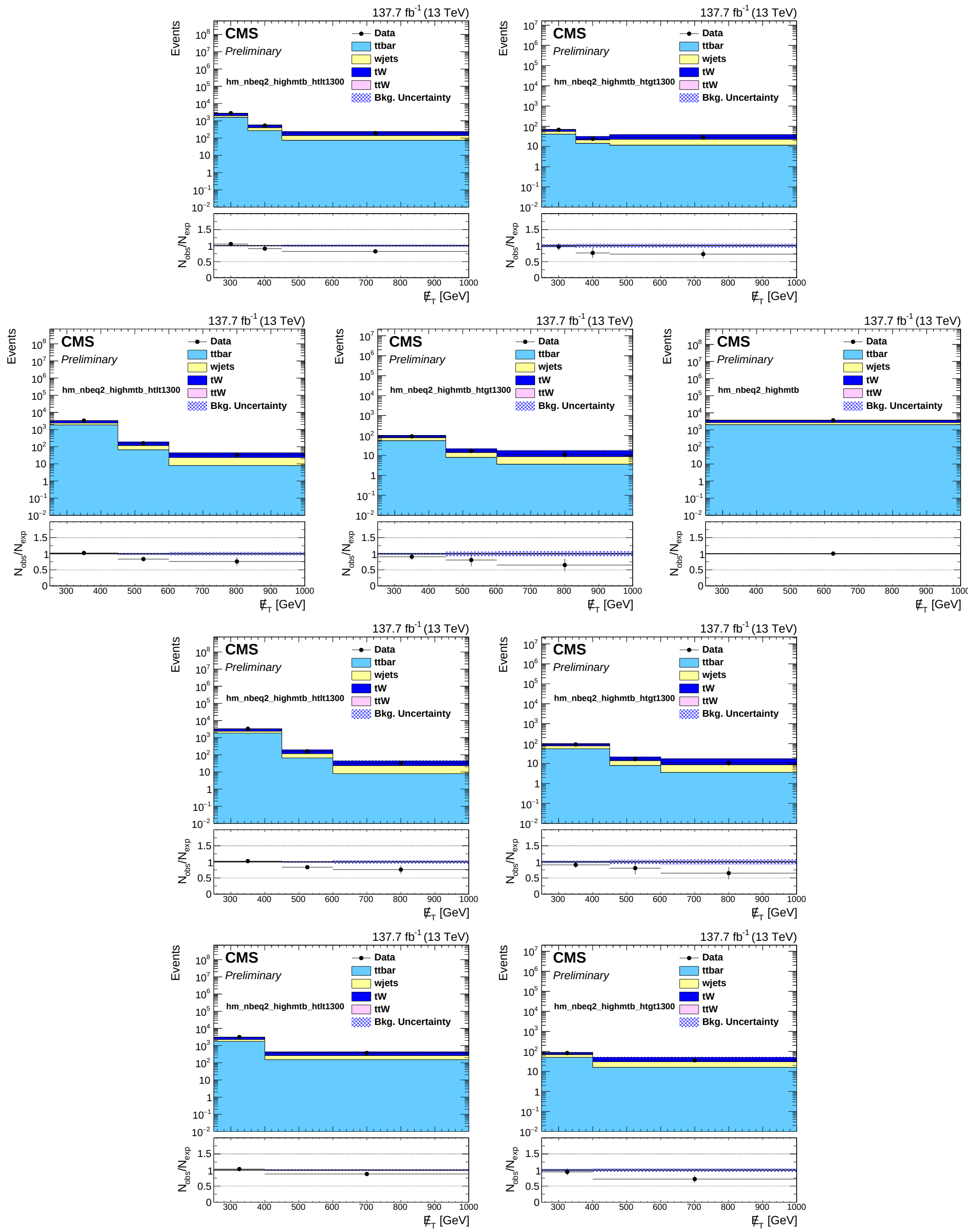

Figure 5.6 : Comparison of the $\not\!\!E_T$ distribution in the single-lepton sample after applying the high Δm baseline selection in the $N_b = 2$ and $N_t = 2, N_{res} = 2$, or $N_W = 2$ region. Data and simulation are represented by the black points and stacked histograms, respectively. The error bars on the ratio of observed data to simulation correspo nd to the data statistical uncertainty and the shaded blue band represents the statistical uncertainty on the simulation. These regions are included with the search regions in the simultaneous fit for the signal extraction in order to estimate the LL contribution.

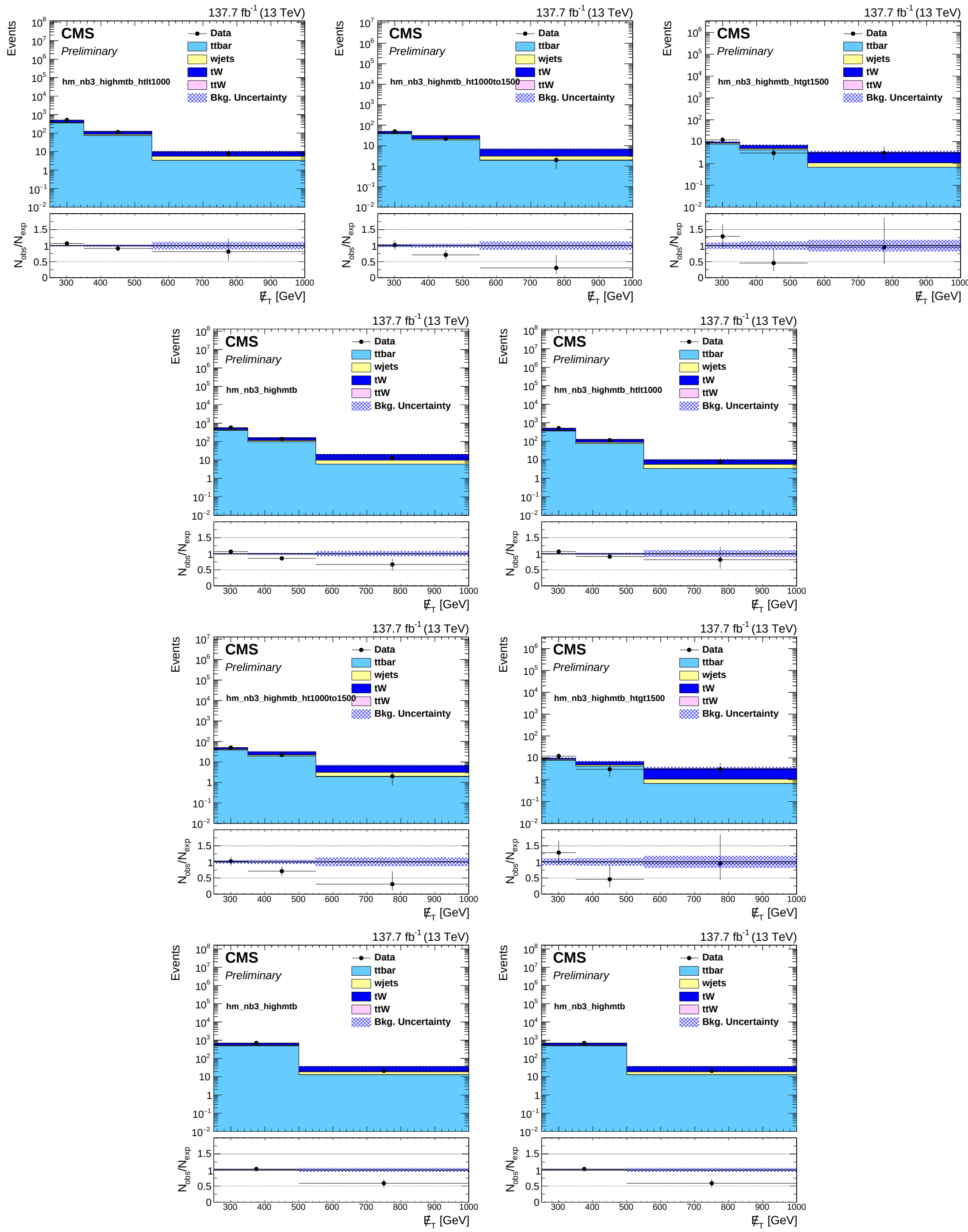

Figure 5.7 : Comparison of the $\not\!\!E_T$ distribution in the single-lepton sample after applying the high Δm baseline selection in the $N_b \geq 3$ and $N_t = 1, N_{res} = 1$, or $N_W = 1$ region. Data and simulation are represented by the black points and stacked histograms, respectively. The error bars on the ratio of observed data to simulation correspo nd to the data statistical uncertainty and the shaded blue band represents the statistical uncertainty on the simulation. These regions are included with the search regions in the simultaneous fit for the signal extraction in order to estimate the LL contribution.

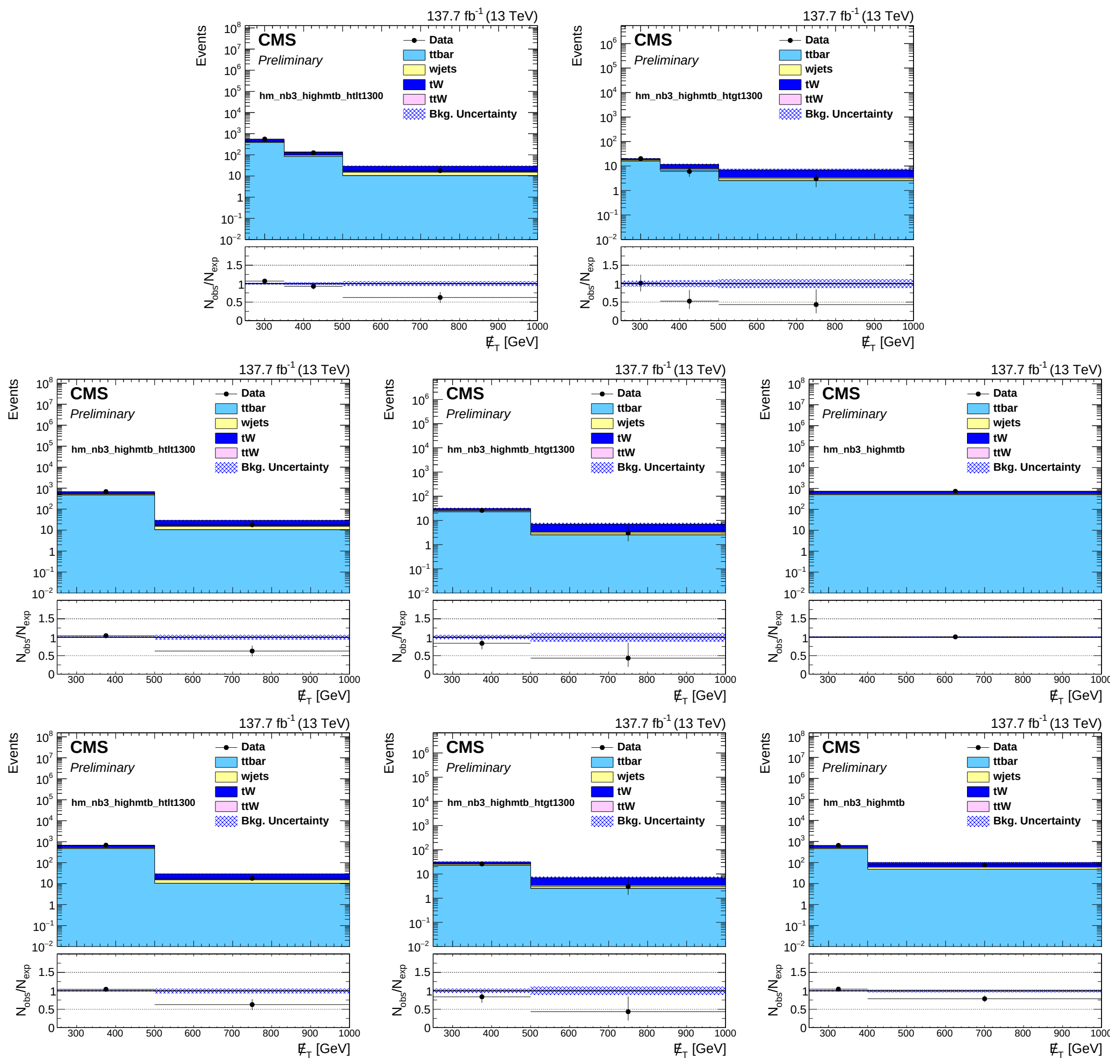

Figure 5.8 : Comparison of the $\not\!\!E_T$ distribution in the single-lepton sample after applying the high Δm baseline selection in the $N_b \geq 3$ $N_t = 2, N_{res} = 2$, or $N_W = 2$ region. Data and simulation are represented by the black points and stacked histograms, respectively. The error bars on the ratio of observed data to simulation correspo nd to the data statistical uncertainty and the shaded blue band represents the statistical uncertainty on the simulation. These regions are included with the search regions in the simultaneous fit for the signal extraction in order to estimate the LL contribution.

Chapter 6

Validation and Estimation

In order to test and validate the background estimation strategy in data, we carry out the background estimation method in a lower $\not\!\!E_T$ region of the zero-lepton sample that is adjacent to the search sample, the "low $\not\!\!E_T$ validation sample", and check the agreement between data and background prediciton. The validaiton sample has significantly larger statistics than the search sample and is signal-depleted. Apart from the difference in the $\not\!\!E_T$ selection, the search selection on the other search variables is applied to the validation sample, with an exception of the regions with more than one top- or W-tags, where relaxed selections (i.e. drop selection in $M_T(b_{1,2}, \not\!\!E_T)$) are applied to gain more statistics. Figgure ? displays the SM estimate and the observed data in the different validation regions. Statistical uncertainties as well as systematic uncertainties resulting from the top- and W-tagging correciton in the background predictions are shown in this plot. The data agrees well with the estimated backgrounds yields within uncertainties.

Bibliography

[1] F. Halzen and A. D. Martin, *Quarks and Leptons: An Introductory Course in Modern Particle Physics.* New York, Usa: Wiley (1984) 396p, 1984.

[2] M. Peskin and D. Schroeder, *An Introduction to quantum field theory.* Addison-Wesley, 1995.

[3] S. Chatrchyan and et al, "Observation of a new boson at a mass of 125 GeV with the CMS experiment at the LHC," *Physics Letters B*, vol. 716, pp. 30–61, Sept. 2012.

[4] S. P. Martin, "A Supersymmetry Primer," *arXiv:hep-ph/9709356*, Sept. 1997. arXiv: hep-ph/9709356.

[5] M. Cacciari, G. P. Salam, and G. Soyez, "The anti-ktjet clustering algorithm," *Journal of High Energy Physics*, vol. 2008, pp. 063–063, Apr. 2008.

[6] "JetID."

[7] "JEC."

[8] D. Griffiths, *Introduction to elementary particles.* Weinheim, Germany: Wiley-VCH (2008) 454 p, 2008.

[9] "BtagRecommendation2016legacy."

[10] "BtagRecommendation94x."

[11] "BtagRecommendation102x."

[12] "InclusiveSecondaryVertexFinder."

[13] B. P. Roe, H.-J. Yang, J. Zhu, Y. Liu, I. Stancu, and G. McGregor, "Boosted Decision Trees as an Alternative to Artificial Neural Networks for Particle Identification," Aug. 2004.

[14] A. Hoecker, P. Speckmayer, J. Stelzer, J. Therhaag, E. von Toerne, H. Voss, M. Backes, T. Carli, O. Cohen, A. Christov, D. Dannheim, K. Danielowski, S. Henrot-Versille, M. Jachowski, K. Kraszewski, A. Krasznahorkay Jr., M. Kruk, Y. Mahalalel, R. Ospanov, X. Prudent, A. Robert, D. Schouten, F. Tegenfeldt, A. Voigt, K. Voss, M. Wolter, and A. Zemla, "TMVA - Toolkit for Multivariate Data Analysis," *arXiv:physics/0703039*, Mar. 2007. arXiv: physics/0703039.

[15] "Search for direct production of top squark pairs decaying to all-hadronic final states in pp collisions at sqrt(s) = 13 TeV - CERN Document Server."